Hadronic B decay reconstruction in Early Phase III data

E. Ganiev[*]

University and INFN, Trieste, Italy

J. Libby, N. Rout[†]

Indian Institute of Technology, Madras, India

D. Tonelli

INFN Trieste, Italy

K. Trabelsi

LAL Orsay, France

Abstract

We report on the validation of early phase III data using hadronic B decays. We reconstruct prominent signals for a variety of $B \to Dh$ decays. A total signal yield of approximately 300 decays is reconstructed in a sample (exp7) corresponding to 0.410 fb^{-1} and proposed for public showing at the EPS 2019 conference. Addition of further data (exp8) and an improved data processing (proc9) allow for reconstructing a total of 2200 decays in 2.69 fb^{-1}, proposed for public showing at the Lepton Photon 2019 conference. This includes observation of the Cabibbo-suppressed $B \to DK$ signal in Belle II data. Study of these signals allows for determining the beam-energy spread from data with approximately 5% precision. Signal yields are moderately (10–20%) inferior to those expected from simulation, with comparable backgrounds, but superior to those obtained in the 2018 pilot commissioning run. These results show a remarkable level of early understanding of detector performance in hadronic final-state reconstruction.

[*]Electronic address: eldar.ganiev@ts.infn.it
[†]Electronic address: niharikarout@physics.iitm.ac.in

Contents

1. INTRODUCTION AND MOTIVATION

The full Belle II detector, complete with its silicon vertex detector, started its first period of collision-data taking on March 11, 2019 and continued until July 1, 2019. The collected sample corresponds to an integrated luminosity of 2.69 fb^{-1} at the $\Upsilon(4S)$ and 0.833 fb^{-1} off resonance. This operation period is conventionally dubbed "(early) Phase III". Fast analysis of these data is essential to validate and benchmark the detector and reconstruction performances.

This note describes validation of the first physics data using various hadronic B meson decays chosen because of their abundance and capability to probe multiple aspects of detector reconstruction (charged and neutral final-state particles, multivertex topologies, long-lived final states etc.). In addition, many of the chosen decays will be relevant signal, or control, channels in many measurements involving B decays to charmed and charmless final states. In what follows, B and D identify generically both charged and neutral mesons.

The reconstruction strategy and procedures are developed and finalized in simulated data prior to applying it to the experimental data. Then, experimental and simulated data are compared in terms of signal yields, background levels, and relevant resolutions. In Section 2, a brief description of the modes reconstructed and the selection is described. The MC performance is discussed in section 4 and 6.

2. SELECTION AND RECONSTRUCTION

We reconstruct the following decay modes:

- $B^{\mp} \to D^0(\to K^-\pi^+, K^-\pi^+\pi^0, K^-\pi^+\pi^-\pi^+)\pi^{\mp}$

- $B^{\mp} \to D^0(\to K^-\pi^+, K^-\pi^+\pi^0, K^-\pi^+\pi^-\pi^+)\rho^{\mp}(\to \pi^{\mp}\pi^0)$

- $B^{\mp} \to D^{*0}[\to D^0(\to K^-\pi^+, K^-\pi^+\pi^0, K^-\pi^+\pi^-\pi^+)\pi^0]\pi^{\mp}$

- $\overline{B}^0 \to D^{*\pm}[\to D^0(\to K^-\pi^+, K^-\pi^+\pi^0, K^-\pi^+\pi^-\pi^+)\pi^{\pm}]\pi^{\mp}$

- $B^0 \to D^-[\to K^+\pi^-\pi^-, K^0_S(\to \pi^+\pi^-)\pi^-]\pi^+$

- $B^0 \to D^-[\to K^+\pi^-\pi^-, K^0_S(\to \pi^+\pi^-)\pi^-]\rho^+(\to \pi^+\pi^0)$

No attempts at optimizing the selection are made, as the goal here is backward with respect to a standard analysis: rather than using the known detector to measure unknown physics, we use known physics to infer the unknown detector performance. We hence use simple selections that do not depend on not-yet-tuned high-level tools and are portable across channels. We first select reconstruction primitives (tracks,...) through baseline quality criteria mainly aimed at rejecting the large contamination from beam-induced backgrounds. These primitives are then combined into $D^{(*)}$ candidates in various final states, which are required to meet simple invariant-mass conditions. Then appropriate additional candidate particles are associated with the $D^{(*)}$ candidates to finalize B candidate reconstruction. We start from the `h+:all` particle list, where h is either a charged kaon or pion and select as follows:

- Transverse impact parameter $|d_0| < 0.5$ cm
  (suppress mismeasured/background tracks)

- Longitudinal impact parameter $|z_0| < 3$ cm
  (suppress mismeasured/background tracks)

- Binary likelihood-ratio kaonID > 0.6 for candidate kaons
  (suppress combinatorial bcgk from pions in kaon candidates)

For the final states containing neutral pions or kaons, we use the `pi0:looseFit` and K^0_S `goodKs` lists. Then, signal candidates meeting the following invariant-mass restrictions are reconstructed through kinematic fits based on the `massKFit` algorithm, a class derived from `KFitBase` that performs kinematic fit imposing constraints on the reconstructed D meson mass using its known value.

- $0.45 < M(\pi^+\pi^-) < 0.55$ GeV/c^2
  (suppress combinatorial bckg) (Fig. 61)

3

- $|M(\pi^+\pi^0) - m_\rho| < 100$ MeV/c^2
  (suppress combinatorial bckg) (Fig. 2)

- $\cos\theta_\rho > -0.8$ (Fig. 3)

- $1.84 < M(K^-\pi^+, K^-\pi^+\pi^0, K^-\pi^+\pi^-\pi^+, K_S^0\pi^0, K_S^0\pi^-\pi^+, K^-K^+) < 1.89$ GeV/c^2
  (suppress combinatorial bckg)

- $1.844 < M(K^-\pi^+\pi^+, K_S^0\pi^+) < 1.894$ GeV/c^2
  (suppress combinatorial bckg) (Fig. 4)

- $0.14 < M(D^0\pi^0) - M(D^0) < 0.144$ GeV/c^2 (suppress combinatorial bckg)

- $0.143 < M(D^0\pi^+) - M(D^0) < 0.147$ GeV/c^2 (suppress combinatorial bckg)

Requirements are imposed on the resulting candidates to enrich the sample in signal fraction

- $5.2 < M_{\rm bc} < 5.29$ GeV/c^2
  (enriched in signal)

- $|\Delta E| < 0.2$ GeV
  (enriched in signal)

- Fox-Wolfram moment ratio R2 $< 0.3(0.25)$ for $B \to D\pi(B \to D\rho)$ candidates
  (suppress continuum). For the observation of $B \to DK$ aimed at LP, a more sophisticated background suppression strategy is used, as described in the next section.

and finally we define the signal region as the two-dimensional cell in energy difference and beam-constrained mass restricted to $|\Delta E| < 0.05$ GeV and $M_{bc} > 5.27$ GeV/c^2.
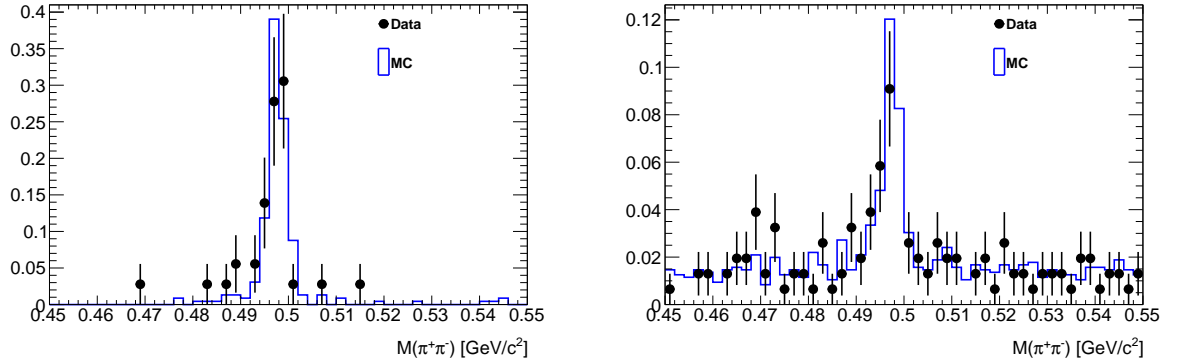

FIG. 1: Normalized distribution of $\pi^+\pi^-$–mass for K_S^0 candidates reconstructed in (circles) experimental and (solid) simulated data with (left) and without (right) the 'goodBelleKs' requirement.
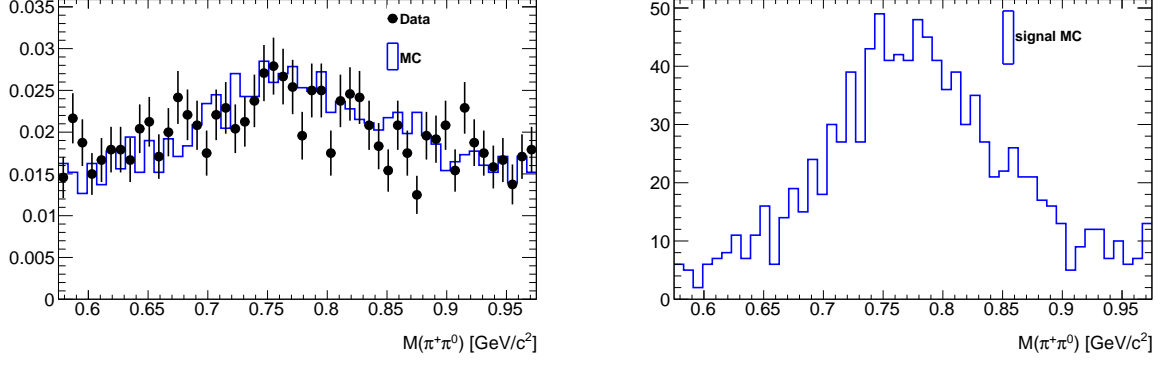
FIG. 2: Normalized distribution of $\pi^+\pi^0$–mass for (left) ρ^0 candidates reconstructed in (circles) experimental and (solid) simulated data. (Right) Distribution of $\pi^+\pi^0$–mass for simulated $B^0 \to D^-\rho^+$ decays.
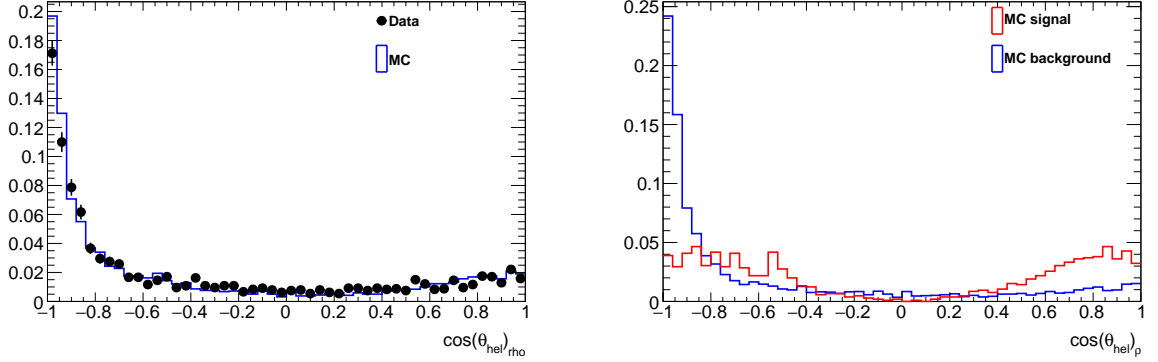

FIG. 3: Distribution of (left) ρ^0 helicity angle for (circles) experimental and (solid) simulated data and (right) breakdown of the simulated distribution in (red) signal and (blue) background components.
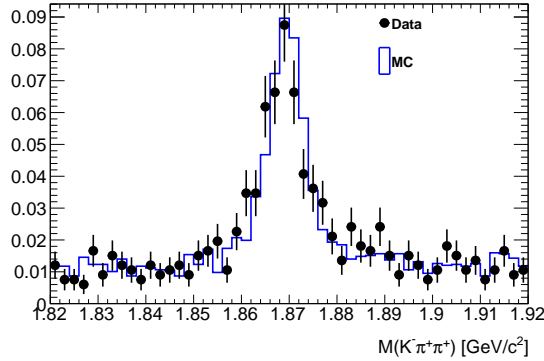

FIG. 4: Normalized distribution of $K^-\pi^+\pi^+$–mass for D^+ candidates reconstructed in (circles) experimental and (solid) simulated data.

3. MULTIVARIATE BACKGROUND SUPPRESSION

The improved data-simulation agreement offered by the proc9 processing allows for a more sophisticated and powerful strategy for suppressing continuum background, which is key to extract a suppressed $B \to DK$ signal. Consistency between off-resonance data and simulation in several discriminating observables known to be effective in separating B signals from continuum background is verified, as shown in Fig. 5. Flavor tagging information and the longitudinal separation of the two vertices in the event are discarded because of significant data-simulation mismodelings. The following topological-discrimination variables are kept and combined in a boosted-decision-tree (FBDT) classifier:

- 16 Kakuno-Super-Fox-Wolfram moments
  (variants of the Fox-Wolfram moments, with improved performance in case of neutral final-state particles, which are sensitive to the 'centrality' of the collective spatial orientations of final-state particles)

- cosTBTO
  (Cosine of the angle between the thrust axis of the signal B candidate and the thrust axis of the rest of the event)

- cosTBz
  (Cosine of the angle between the thrust axis of the signal B candidate and the beam axis.)

- B_{thrust}
  (Magnitude of the signal B thrust axis)

- $\cos \theta_B$
  (cosine of the angle θ_B between the reconstructed momentum of the B candidate in the $\Upsilon(4S)$ reference frame and the beam axis.)

The FBDT is trained to classify signal from background using simulated $B \to D\pi$ events where the Monte-Carlo truth "IsSignal" variable defines the training target. Performance is tested on independent samples of simulated $B \to D\pi$ events. The FBDT receiver-operating-characteristic (ROC) is shown in the left panels of Fig. 7 for $B^+ \to D\pi^+$ decays and Fig. 8 for $B^0 \to D\pi^+$ decays. The optimal FBDT threshold is found by finding, in the space of FBDT, the subset of events that maximizes the figure of merit $N_S/\sqrt{N_S + N_B}$, where N_S is the $B \to DK$ yield and N_B is the background yield, both determined in the signal region $-0.08 < \Delta E < -0.02$. While the chosen figure of merit is strictly optimal in minimizing signal-yield variance only in a counting experiment of a narrow signal over a uniform background, it still offers a reasonably optimal approximation in our case. The figure-of-merit values as functions of FBDT output are shown in the right panels of Fig. 7 for $B^+ \to D\pi^+$ decays and Fig. 8 for $B^0 \to D\pi^+$ decays. The resulting choices are FBDT > 0.94, which rejects 95.5% of background while retaining 50% of $B^+ \to DK^+$ signal and FBDT > 0.92 which retains 65% of $B^0 \to DK^+$ signal while rejecting 96% of background.

Data/MC comparison and continuum MC/off-resonance data comparisons for FBDT output are shown in Fig. 9.
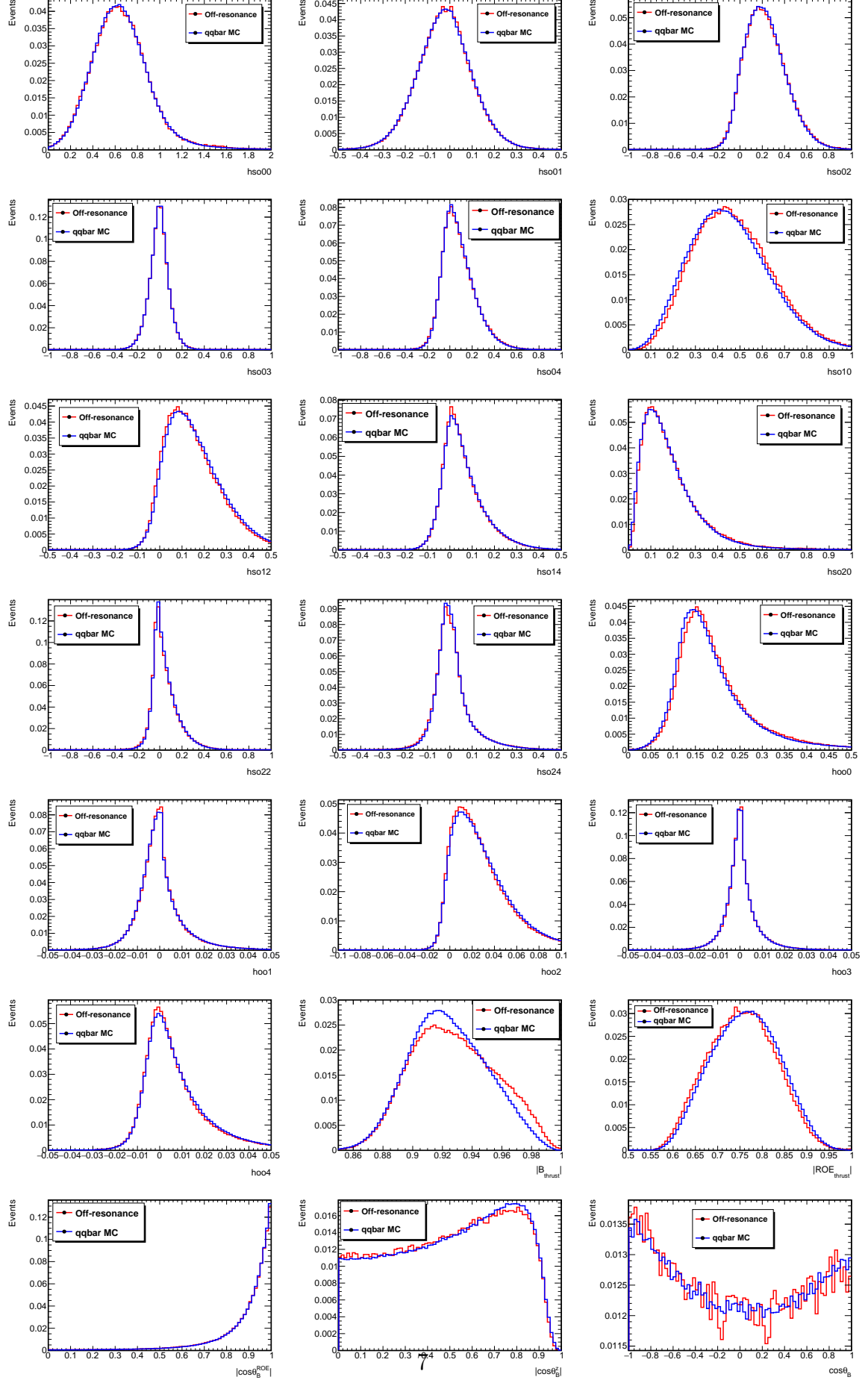
6

FIG. 5: Distributions of continuum-suppression discriminating variables for (blue) simulated $q\bar{q}$ events compared with (red) off-resonance data.
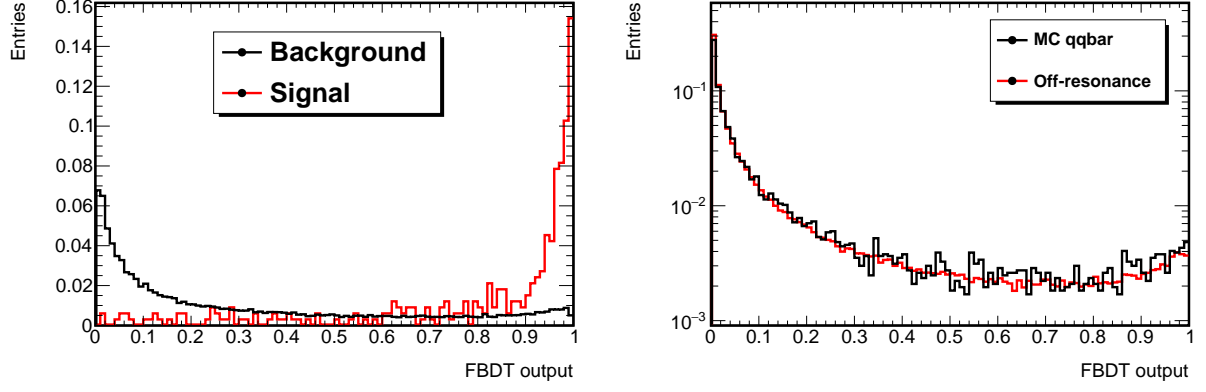
FIG. 6: Distribution of FBDT classifier output for simulated-test-sample $B^+ \to DK^+$ decays (left) and comparison of the FBDT distribution in simulated $q\bar{q}$ data and the off-resonance experimental data in log scale (right).
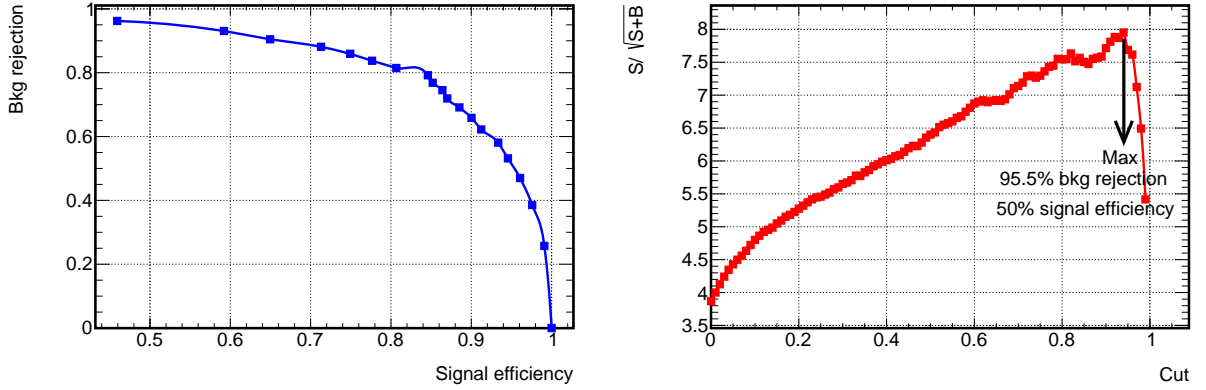

FIG. 7: Background-rejection as a function of $B^+ \to DK^+$ signal efficiency for various lower thresholds on the FBDT classifier (left). Figure of merit for $B^+ \to DK^+$ decays as a function of FBDT threshold (right). Both curves are evaluated in simulated test-sample data.
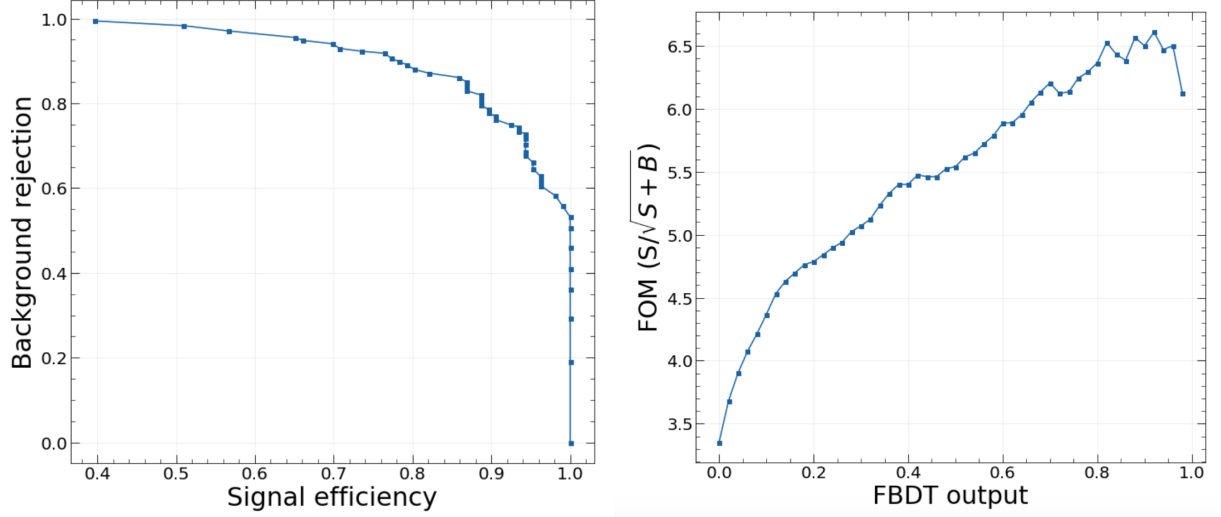
FIG. 8: Background-rejection as a function of $B^0 \to D^- K^+$ signal efficiency for various lower thresholds on the FBDT classifier (left). Figure of merit for $B^0 \to D^- K^+$ decays as a function of FBDT threshold (right). Both curves are evaluated in simulated test-sample data.
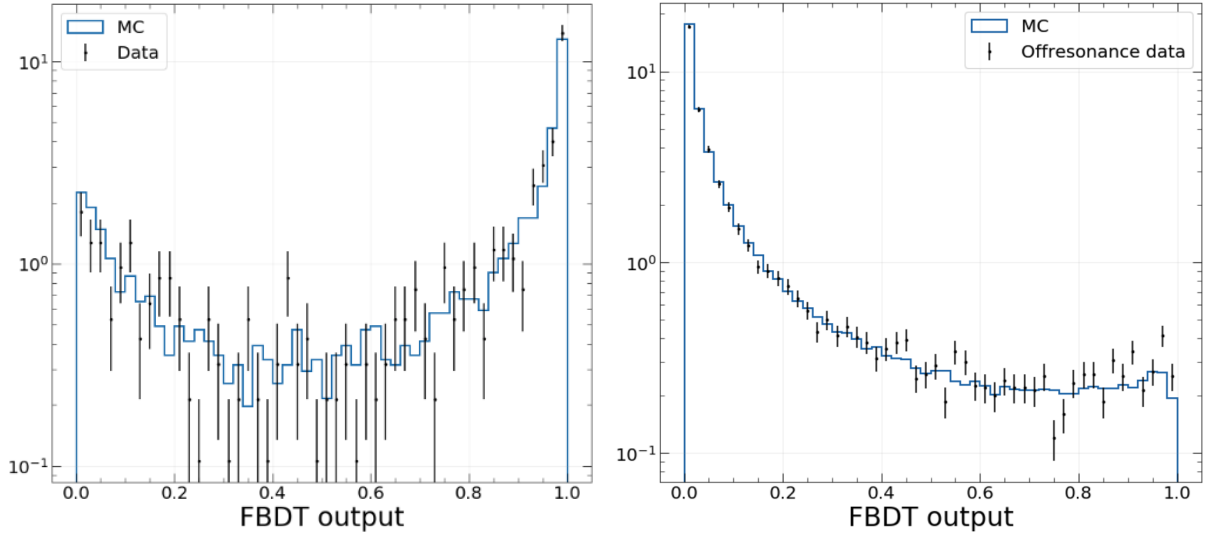

FIG. 9: Distribution of FBDT output for (left) $B^0 \to D\pi$ candidates restricted to the signal region $|\Delta E| < 0.05$ GeV and $M_{\rm bc} > 5.27$ GeV/c^2 with corresponding distribution from simulation overlaid and (right) same thing but for off-resonance data.

4. SIGNAL YIELDS IN SIMULATED DATA

We first apply the reconstruction in a MC12 sample corresponding to 10 fb^{-1} to estimate the expected signal yields and derive mass models for the yield fits. The shapes used in all fits are empirical and chosen based on the adequacy to model the simulated data. Figures 14, 15 and 16 shows fit projections for the $B^0 \to D^-(\to K^+\pi^-\pi^-)\pi^+$, $B^0 \to D^-(K_S^0\pi^-)\pi^+$ and $B^0 \to D^-(K^+\pi^-\pi^-)\rho^+$ candidates, respectively.
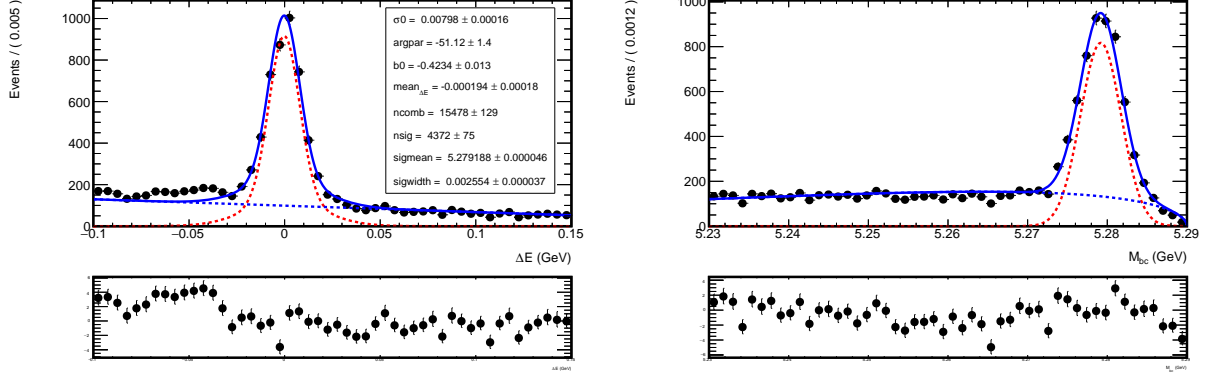

FIG. 10: Distribution of ΔE (left) and M_{bc} (right) for $B^- \to D^0\pi^-$ candidates reconstructed from a simulated MC12 on-resonance sample, with fit results and pulls overlaid.
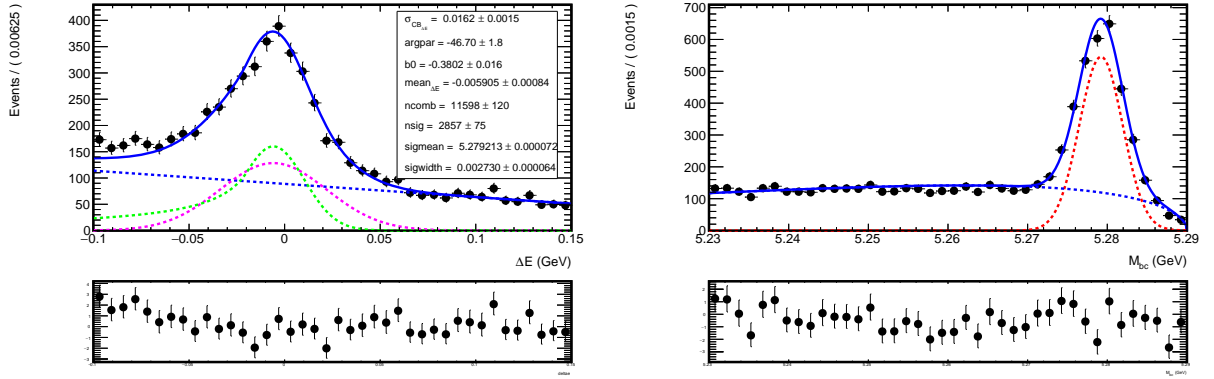

FIG. 11: Distribution of ΔE (left) and M_{bc} (right) for $B^- \to D^0\rho^-$ candidates reconstructed from a simulated MC12 on-resonance sample, with fit results and pulls overlaid.

10
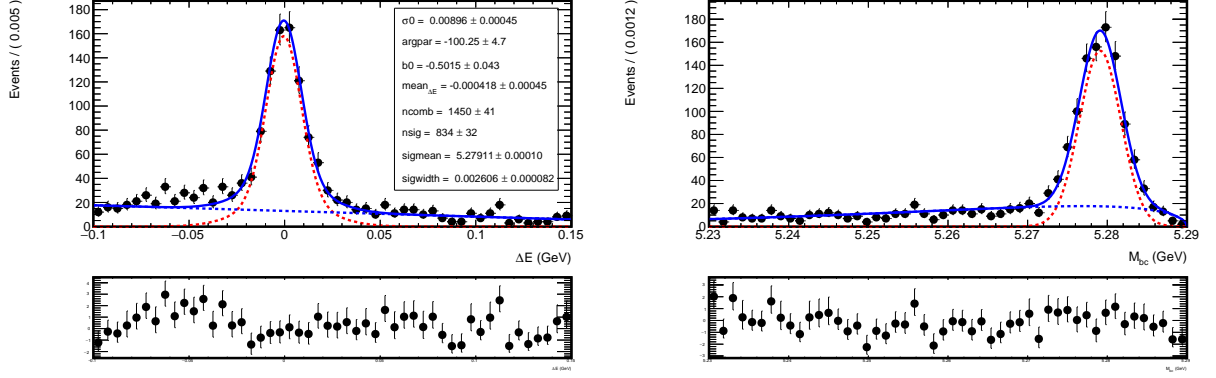
FIG. 12: Distribution of ΔE (left) and M_{bc} (right) for $B^- \to D^{*0}\pi^-$ candidates reconstructed from a simulated MC12 on-resonance sample, with fit results and pulls overlaid.
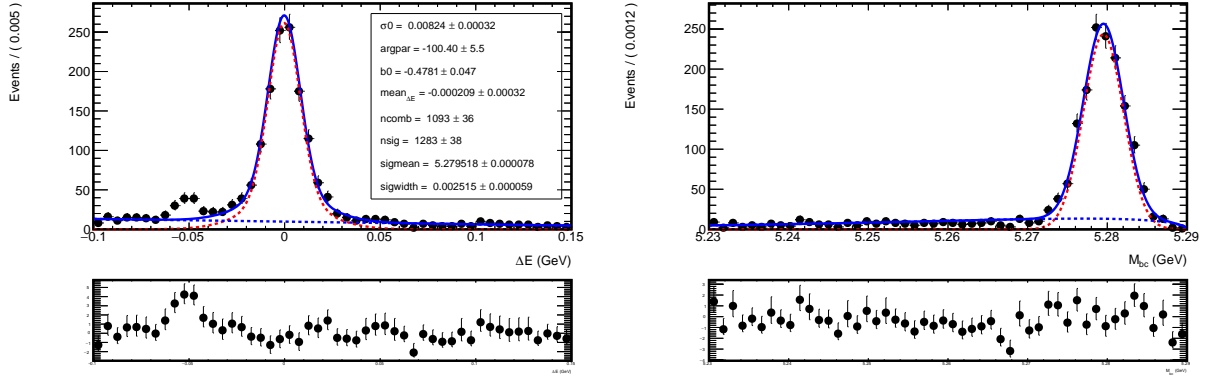

FIG. 13: Distribution of ΔE (left) and M_{bc} (right) for $B^0 \to D^{*-}\pi^+$ candidates reconstructed from a simulated MC12 on-resonance sample, with fit results and pulls overlaid.

A RooPlot of "M$_{bc}$ (GeV/c^2)"

bckg_yield = 3947 ± 66
frac_de = 0.079 ± 0.012
signal_yield = 1235 ± 40

A RooPlot of "ΔE (GeV)"
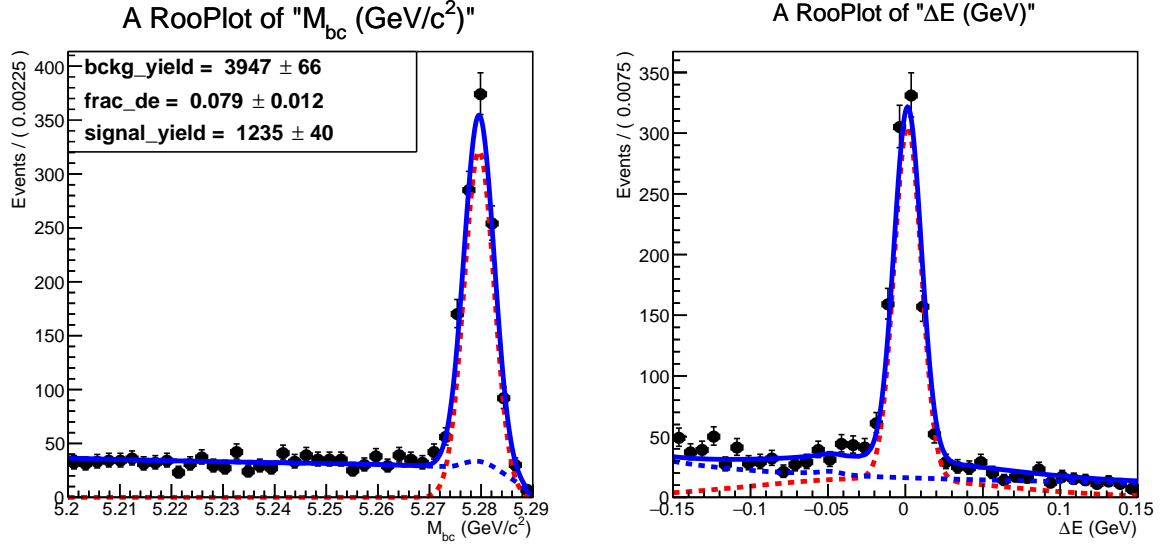
FIG. 14: Distribution of ΔE and M_{bc} for $B^0 \to D^-(K^+\pi^-\pi^-)\pi^+$ candidates reconstructed from a simulated MC12 on-resonance sample.

A RooPlot of "M$_{bc}$ (GeV/c^2)"

bckg_yield = 296 ± 18
frac_de = 0.080 ± 0.047
signal_yield = 89 ± 10

A RooPlot of "ΔE (GeV)"

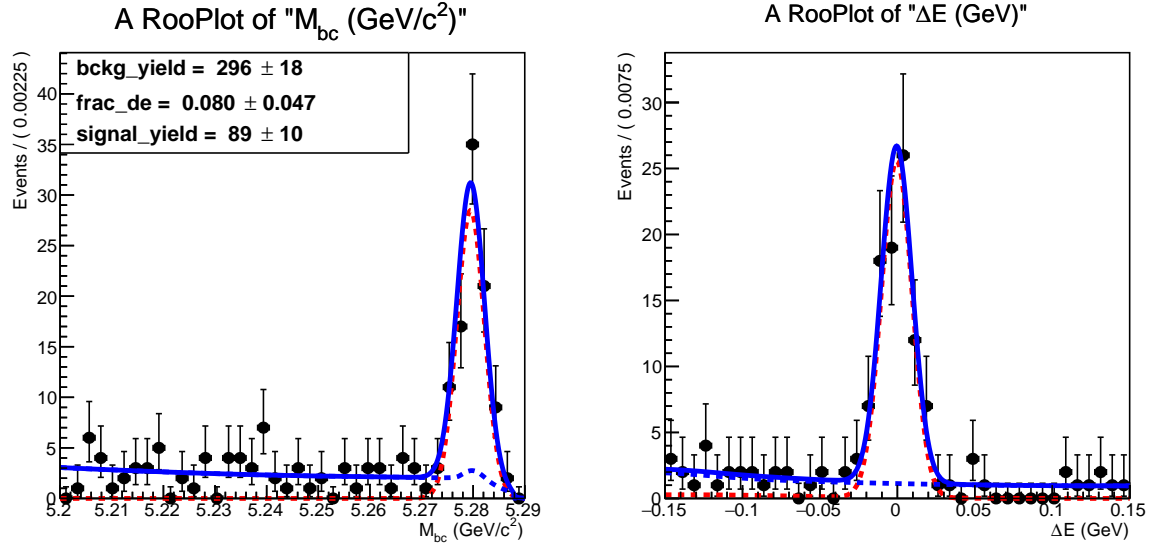FIG. 15: Distribution of ΔE and M_{bc} for $B^0 \to D^-(K_S^0\pi^-)\pi^+$ candidates reconstructed from a simulated MC12 on-resonance sample.

A RooPlot of "M$_{bc}$ (GeV/c^2)"

bckg_yield = 3972 ± 67
frac_de = 0.393 ± 0.035
signal_yield = 673 ± 35

A RooPlot of "ΔE (GeV)"
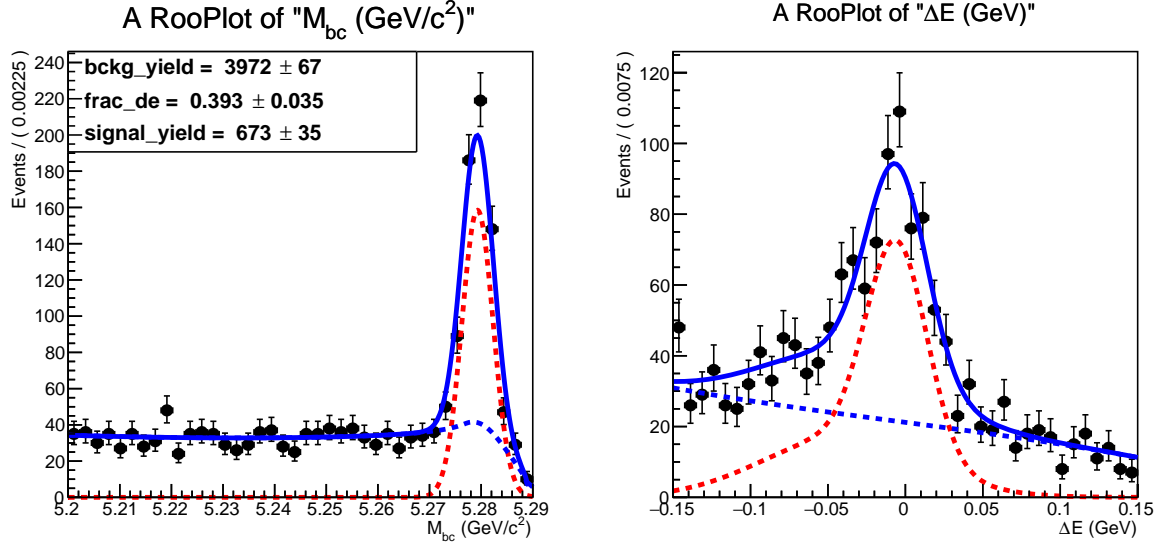
FIG. 16: Distribution of ΔE and M_{bc} for $B^0 \to D^-(K^+\pi^-\pi^-)\rho^+$ candidates reconstructed from a simulated MC12 on-resonance sample.

5. SIGNAL YIELDS IN EXPERIMENTAL DATA

The fit model determined from simulation is then applied to the experimental data with appropriate combinations of fixed and floating parameters that take into account varying channel-dependent sample sizes. In addition, peak positions are allowed to float and multiplicative scale ('fudge') factors are applied to the peak widths , when appropriate to allow for minor data-simulation mismatches. Generally, such factors are determined from data in the large-yield channels and applied in the low-yield ones. We determine the yields of each channel through two-dimensional fits of the ΔE and $M_{\rm bc}$ distributions. Fit models vary from one channel to another but in general we use:

- **Signal** single Gaussian distributions in $M_{\rm bc}$ and double Gaussian distributions (or Gaussian plus Crystal ball) in ΔE.

- **Continuum background** Argus function or Argus summed to a polynomial function in $M_{\rm bc}$ and low-order polynomial functions in ΔE.

- **Peaking background** Crystal ball in $M_{\rm bc}$ and Gaussian functions or low-order polynomial functions in ΔE.

Since not all data were simultaneously available with the latest set of calibrations, we analyzed chunks of data separately as soon as they became available.

5.1. Official exp7 bucket4 data

The first official data set for Phase III is conventionally dubbed "experiment7-bucket4" and corresponds to a luminosity of 68 pb^{-1} (run ranges 1135–1155 and 1375–1587). Because of the small sample size, we choose not to show distributions for this data set only. However, yields determined for the experiment7 data set include candidates reconstructed in bucket4 (Tables I and II).

5.2. Official exp7 bucket6 data

The chunk referred to as "experiment7-bucket6" corresponds to an integrated luminosity of 344 pb^{-1}. Figures 17, 19, 20, 22, 24 and 25 show the ΔE and M$_{bc}$ distributions for $B^+ \to D\pi^+$, $B^+ \to D\rho^+$, $B^- \to D^{*0}\pi^-$, $\overline{B}^0 \to D^{*\pm}\pi^{\mp}$, $B^0 \to D^-\pi^+$ and $B^0 \to D^-\rho^+$ decays, respectively, in these data. Table I shows signal yields resulting from the ΔE fits. All fit parameters are fixed to the values determined in simulation, except for the signal peak position and for an additional free scale factor applied to the $B \to D\pi$ width. We don't have a signal yield for $B \to D\rho$ because the narrow signal peak is mostly dominated by large combinatorial background. Mass distributions in experiment7-bucket6 data are shown in figure 18, 21 and 23 with fit functions and residuals overlaid.

5.3. Unofficial exp8 data

In early July 2019 another large chuck of data was available for unofficial analysis although it wasn't processed with the most updated set of calibration constants and conditions. These
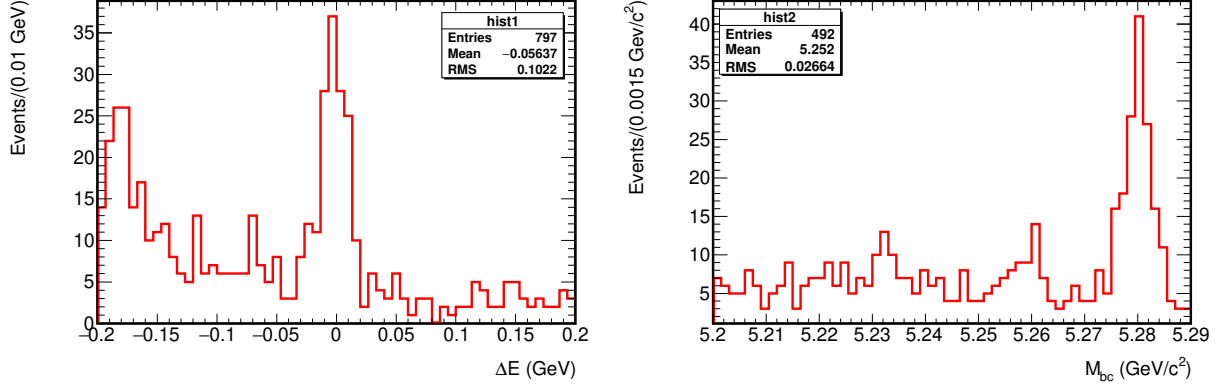
FIG. 17: Distributions of (left) ΔE and (right) and M$_{bc}$ for $B^+ \to D\pi^+$ candidates reconstructed in bucket6 data.
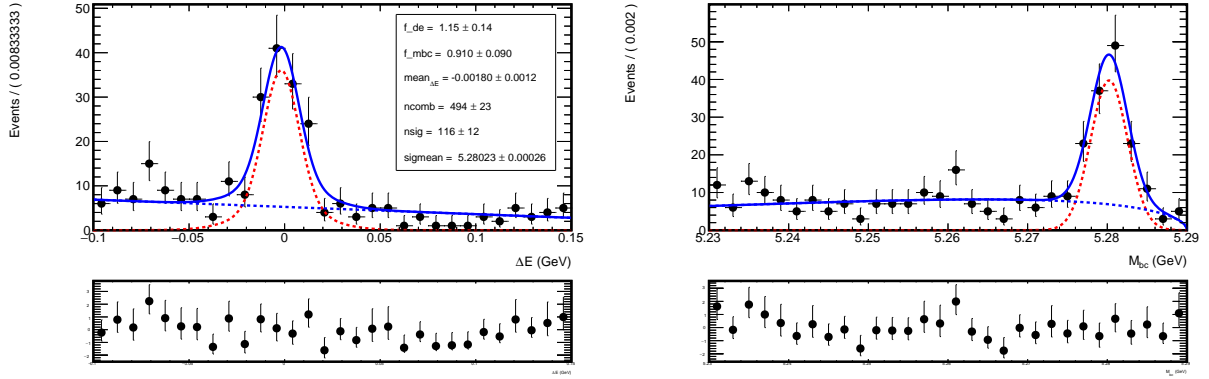

FIG. 18: Distribution of ΔE and M$_{bc}$for $B^+ \to D\pi^+$ candidates reconstructed in bucket6 data, with fit projections and overlaid and pulls.

data, collected in runs 43–2249 and corresponding to an integrated luminosity of 1.8 fb^{-1}, are dubbed "experiment 8". Figures 26, 28, 30, 32, 34 and 35 show the ΔE and M$_{bc}$ distributions for $B \to D\pi$, $B \to D\rho$, $B \to D^{*0}\pi$, $B^0 \to D^{*\pm}\pi$, $B^0 \to D^-\pi^+$ and $B^0 \to D^-\rho^+$ candidates, respectively, reconstructed in such experiment8 data. Table ?? reports the corresponding signal yields as resulting from fits to the ΔE distribution. Fit parameters are fixed from simulation except for the signal peak position and a scale factor on its width (Figures 27, 29, 31, 33, 36 and 37.)

5.4. Official exp7 and exp8 data processed through proc9

.

Figures 38, 39, 40, and 41 show ΔE and M$_{bc}$ distributions, with fit projections overlaid, for $B^+ \to D\pi^+$, $B^+ \to D\rho^+$, $B^- \to D^{*0}\pi^-$ and $B^0 \to D^{*\pm}\pi^{\mp}$ candidates, respectively, reconstructed in exp7 proc9 data. Figures 42, 43, 44 and 45 show the corresponding distributions
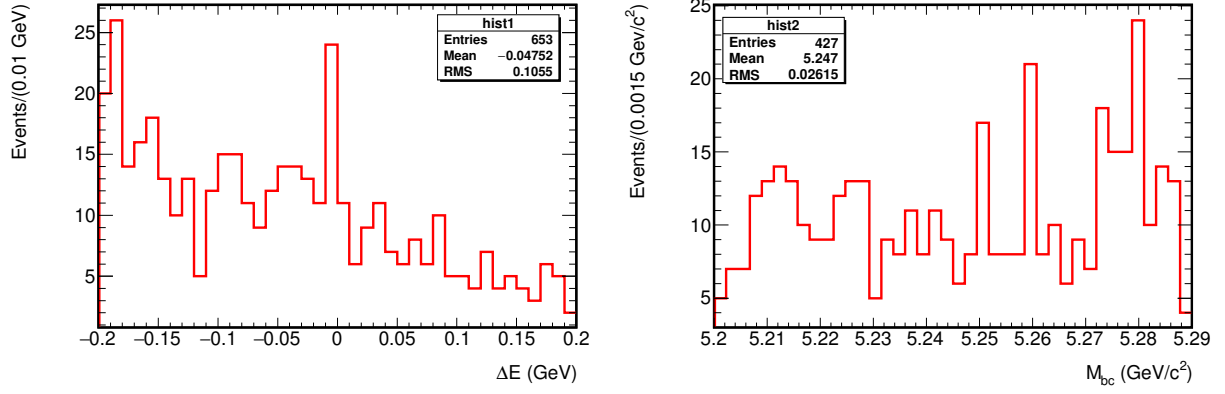
15

FIG. 19: Distributions of (left) ΔE and (right) and M_{bc} for $B^+ \to D\rho^+$ candidates reconstructed in bucket6 data.
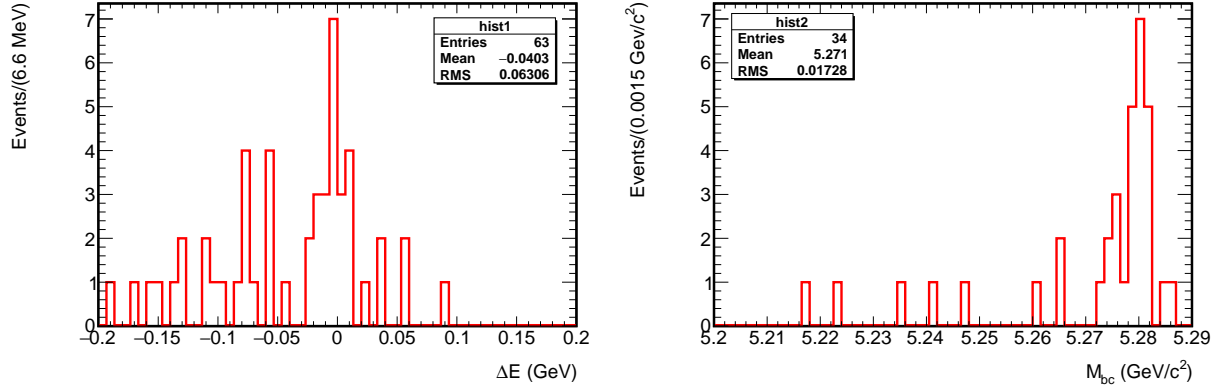

FIG. 20: Distributions of (left) ΔE and (right) and M_{bc} for $B^- \to D^{*0}\pi^-$ candidates reconstructed in bucket6 data.

for candidates reconstructed in exp8 proc9 data. Figures 46, 47, and 48 show ΔE and M_{bc} distributions, with fit projections overlaid, for $B^0 \to D^-(K^+\pi^-\pi^-)\pi^+$, $B^0 \to D^-(K_S^0\pi^-)\pi^+$, and $B^0 \to D^-(K^+\pi^-\pi^-)\rho^+$ candidates, respectively, reconstructed in exp7 proc9 data. Figures 49, 50 and 51 shows the corresponding distributions for candidates reconstructed in exp8 proc9 data.
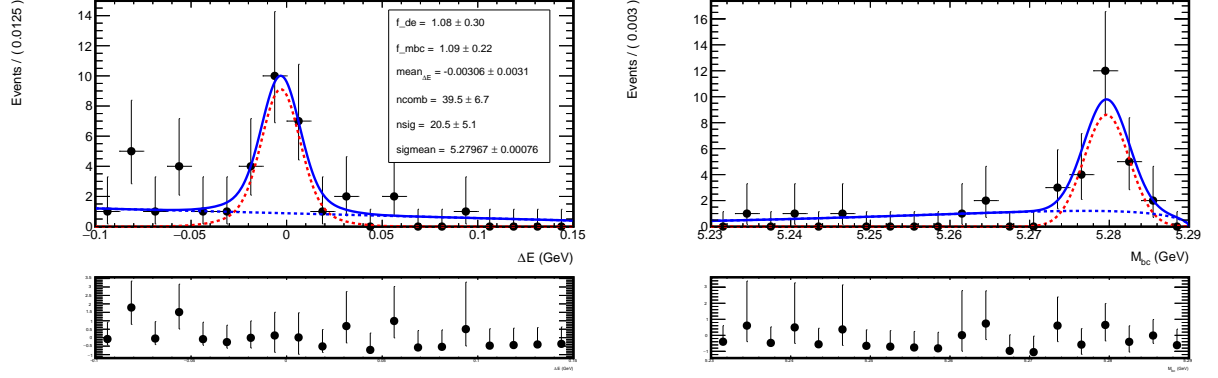
16

FIG. 21: Distribution of ΔE and M_{bc} for $B^- \to D^{*0}\pi^-$ candidates reconstructed in bucket6 data, with fit projections and overlaid and pulls.
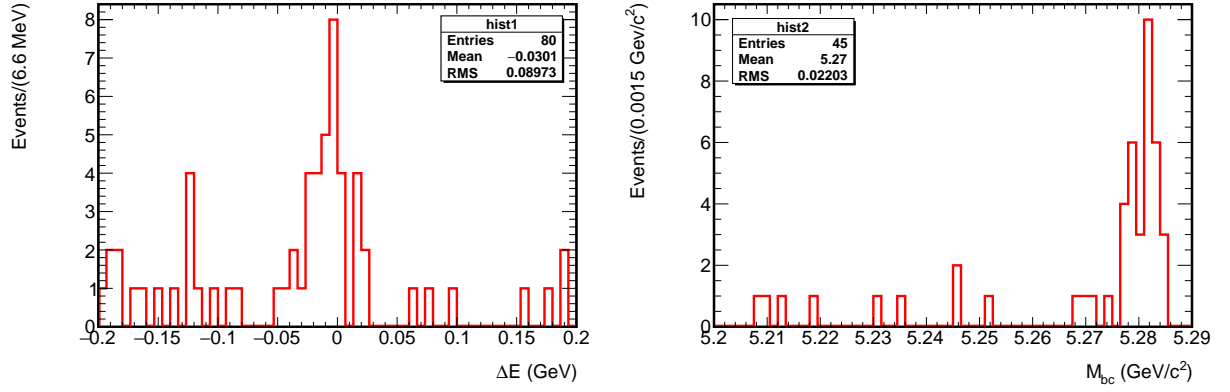

FIG. 22: Distributions of (left) ΔE and (right) and M_{bc} for $^0 \to D^{*\mp}\pi^\pm$ candidates reconstructed in bucket6 data.
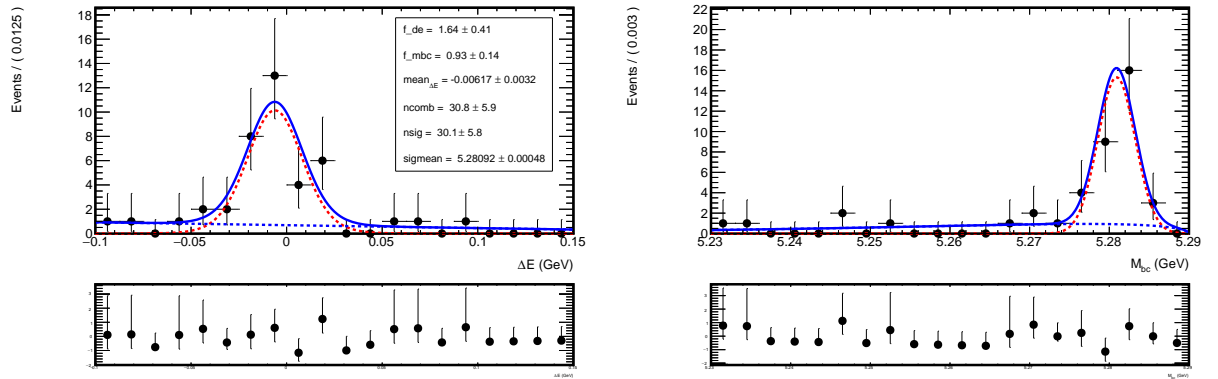

FIG. 23: Distribution of ΔE and M_{bc} for $B^0 \to D^{*\pm}\pi^\mp$ candidates reconstructed in bucket6 data, with fit projections and overlaid and pulls.
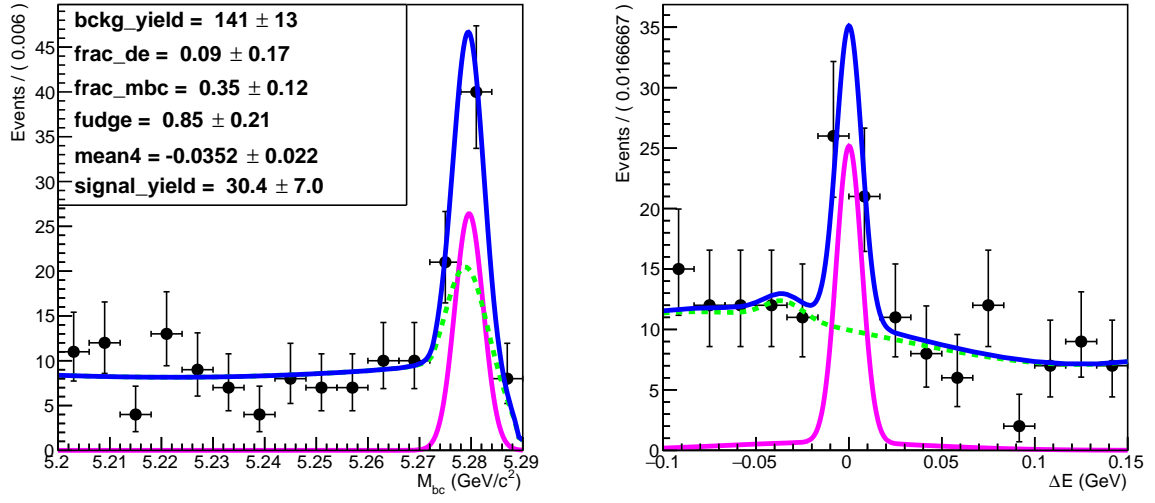
17

FIG. 24: Distribution of ΔE and M_{bc} for $B^0 \to D^- \pi^+$ candidates in bucket6 data.
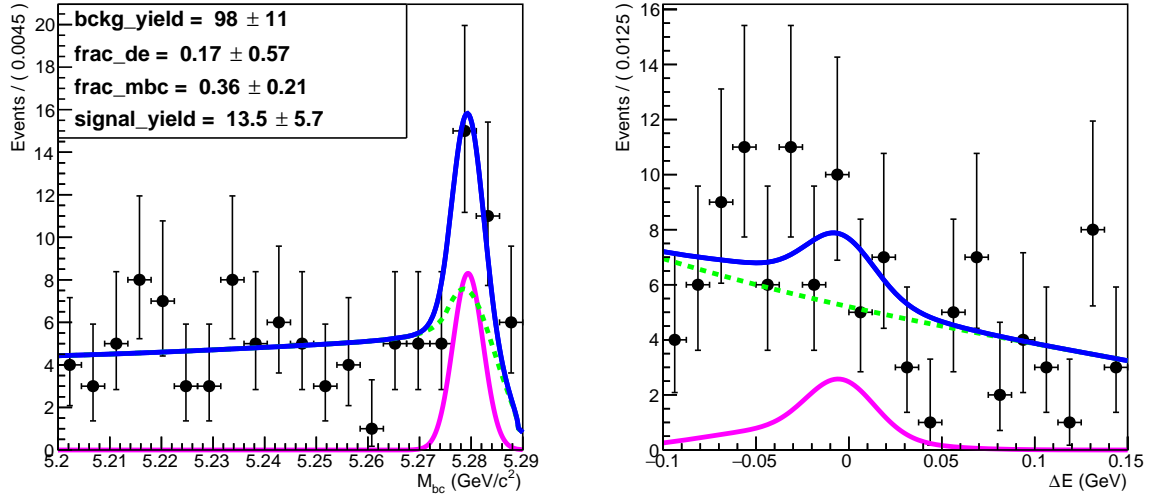

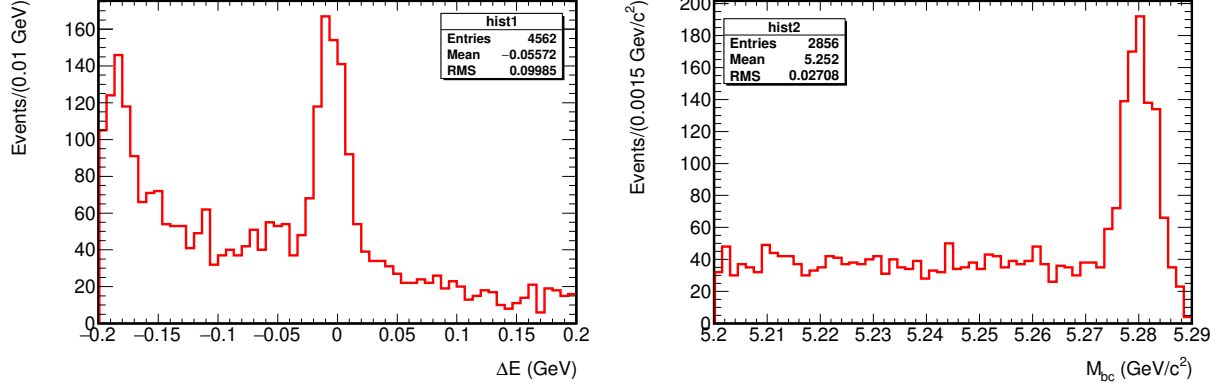FIG. 25: Distribution of ΔE and M_{bc} for $B^0 \to D^- \rho^+$ candidates in bucket6 data.

FIG. 26: Distributions of (left) ΔE and (right) and M_{bc} for $B^+ \to D\pi$ candidates reconstructed in unofficial exp8 data (runs 43–2249).

FIG. 27: Distribution of ΔE and M_{bc} for $B^+ \to D\pi$ candidates reconstructed in unofficial exp8 data (runs 43–2249) with fit projection overlaid and pulls.

FIG. 28: Distributions of (left) ΔE and (right) and M_{bc} for $B^+ \to D\rho$ candidates reconstructed in unofficial exp8 data (runs 43–2249).
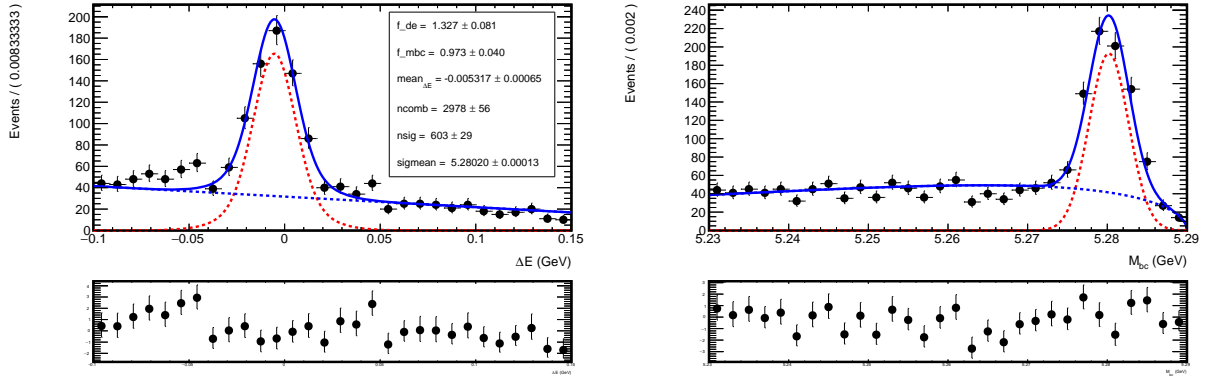
FIG. 29: Distribution of ΔE and M_{bc} for $B^+ \to D\rho$ candidates reconstructed in unofficial exp8 data (runs 43–2249) with fit projection overlaid and pulls.

FIG. 30: Distributions of (left) ΔE and (right) and M_{bc} for $B^+ \to D^{*0}\pi$ candidates reconstructed in unofficial exp8 data (runs 43–2249).

FIG. 31: Distribution of ΔE and M_{bc} for $B^+ \to D^{*0}\pi$ candidates reconstructed in unofficial exp8 data (runs 43–2249) with fit projection overlaid and pulls.
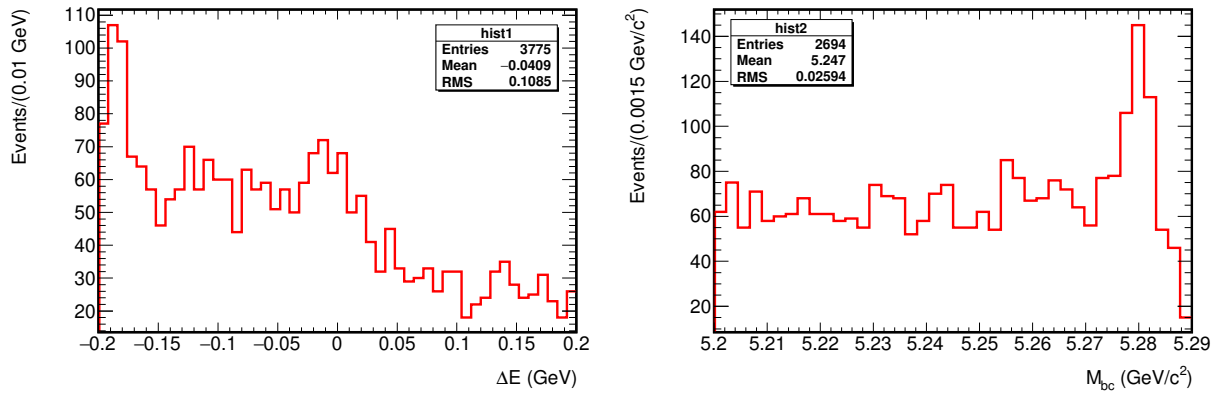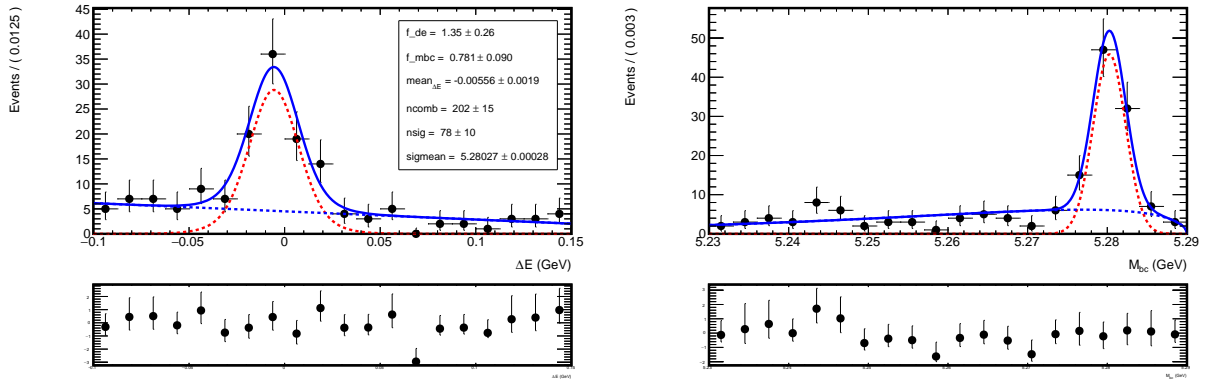
20

FIG. 32: Distributions of (left) ΔE and (right) and M_{bc} for $B^+ \rightarrow D^{*\pm}\pi$ candidates reconstructed in unofficial exp8 data (runs 43–2249).

FIG. 33: Distribution of ΔE and M_{bc} for $B^+ \rightarrow D^{*\pm}\pi$ candidates reconstructed in unofficial exp8 data (runs 43–2249) with fit projection overlaid and pulls.
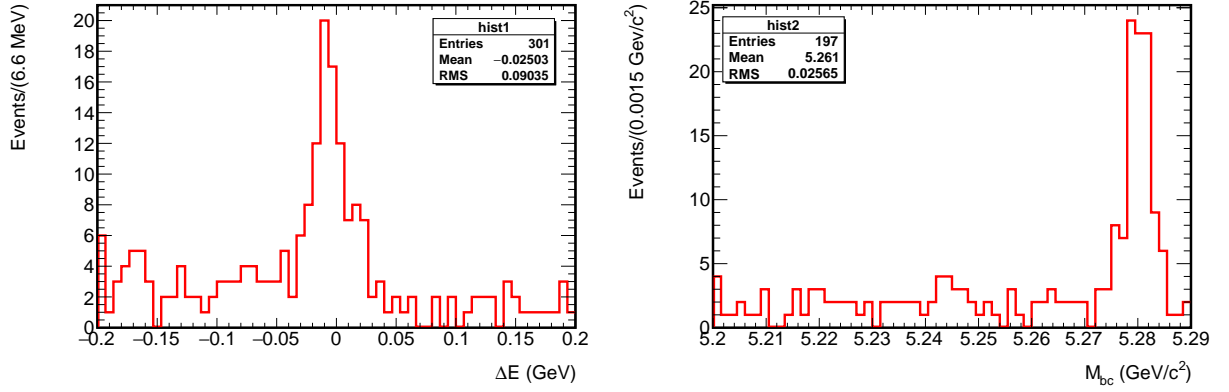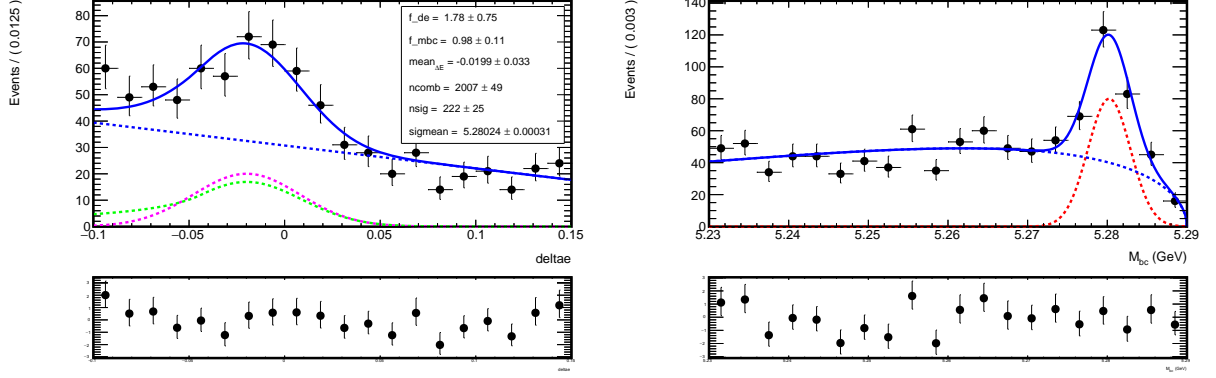
FIG. 34: Distributions of (left) ΔE and (right) and M_{bc} for $B^0 \to D^-\pi^+$ candidates reconstructed in unofficial exp8 data (runs 43–2249).

FIG. 35: Distributions of (left) ΔE and (right) and M_{bc} for $B^0 \to D^-\rho^+$ candidates reconstructed in unofficial exp8 data (runs 43–2249).
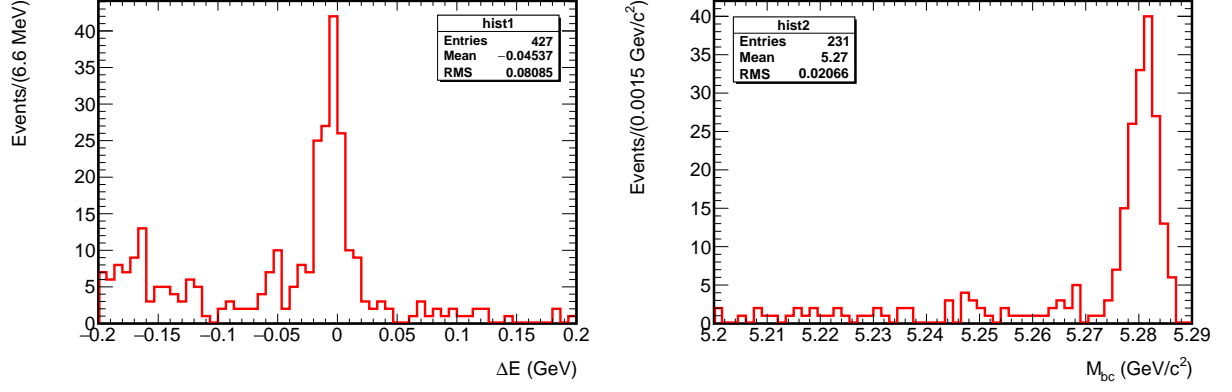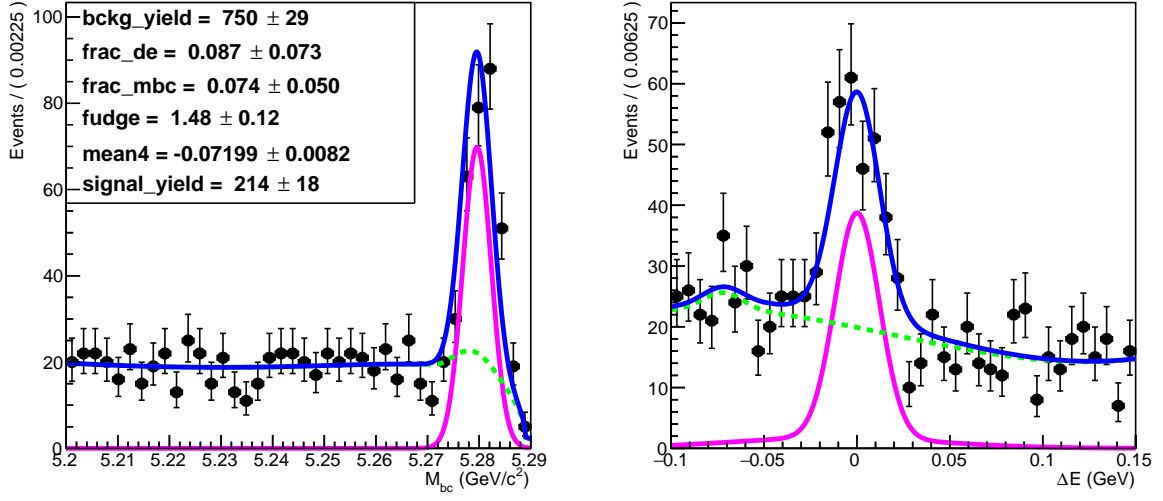
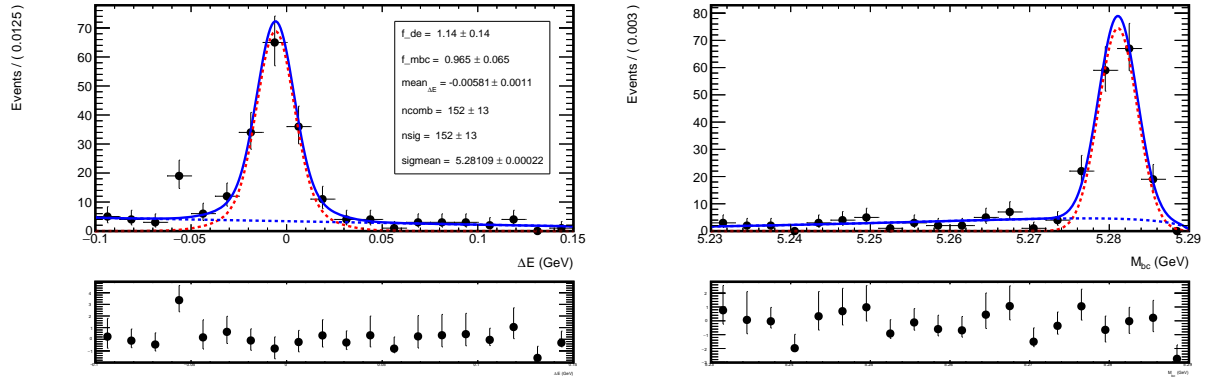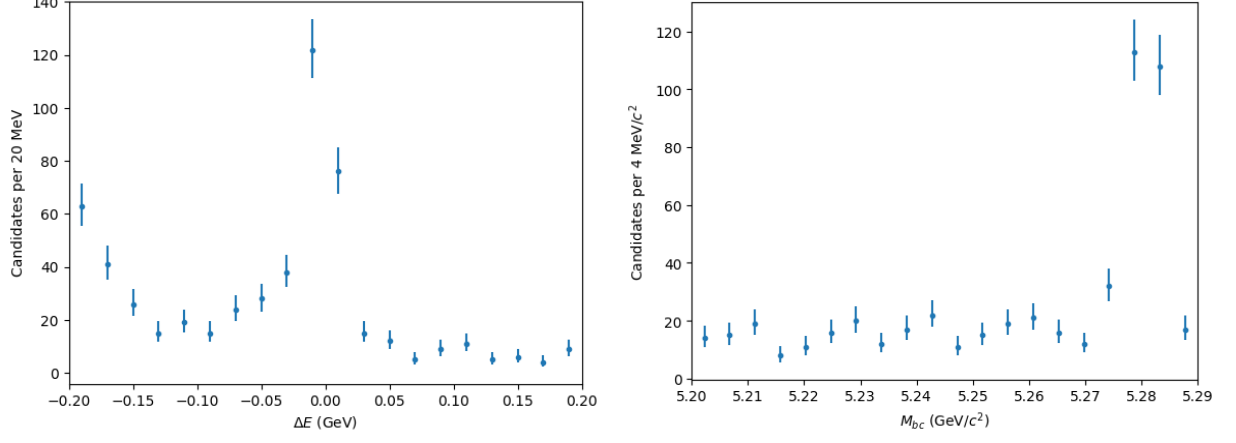FIG. 36: Distribution of ΔE and M_{bc} for $B^0 \to D^-\pi^+$ candidates in unofficial exp8 data (runs 43–2249) with fit projections overlaid.
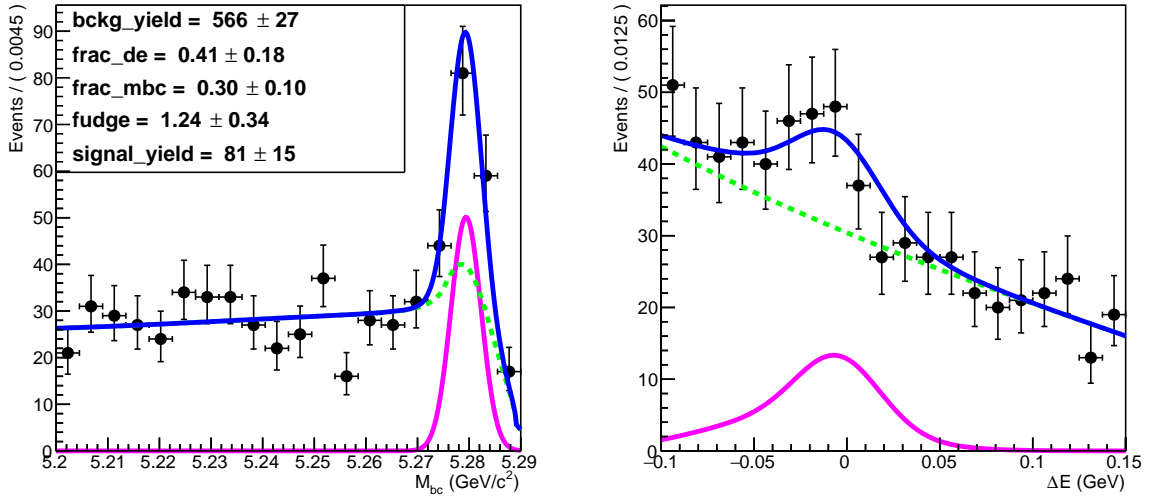
FIG. 37: Distribution of ΔE and M_{bc} for $B^0 \to D^-\rho^+$ candidates in unofficial exp8 data (runs 43–2249) with fit projections overlaid.

FIG. 38: Distributions of (left) ΔE and (right) and M_{bc} for $B^+ \to D\pi$ candidates reconstructed in official exp7 proc9 data.
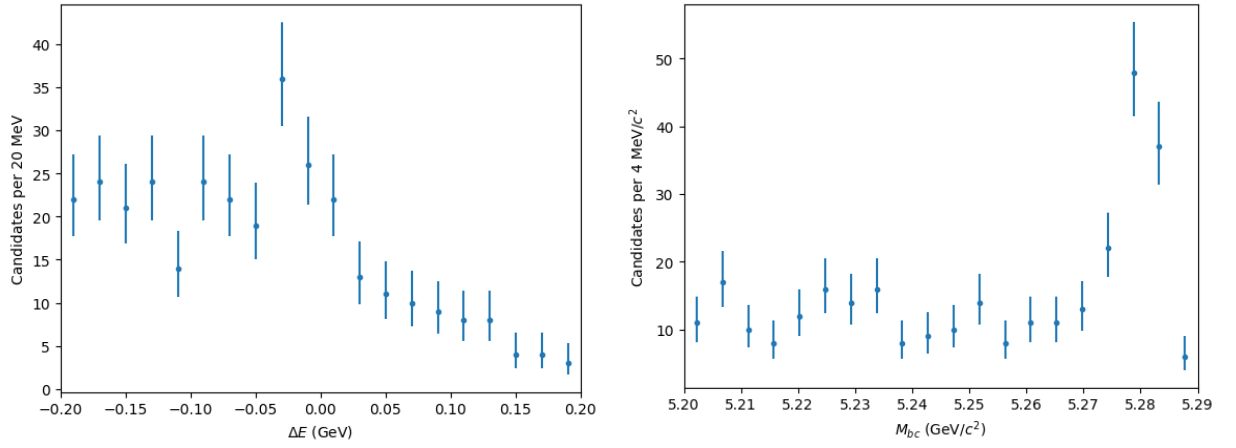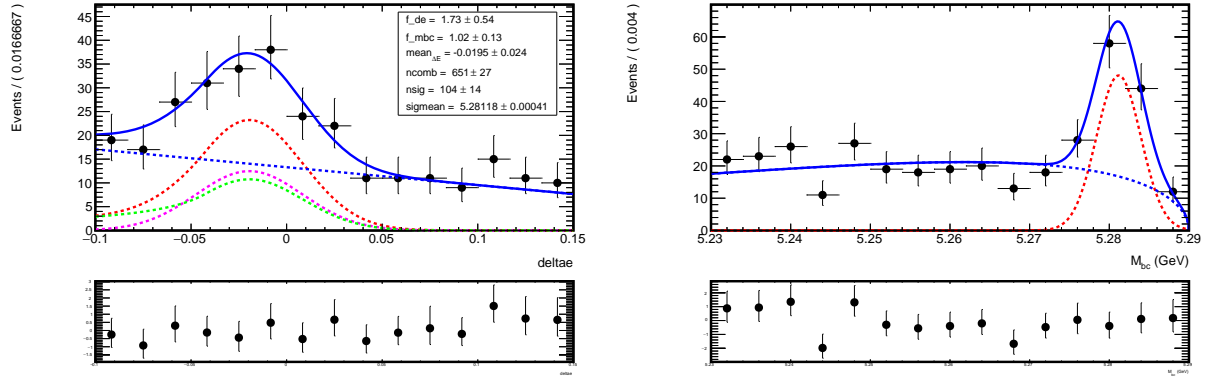

FIG. 39: Distributions of (left) ΔE and (right) and M_{bc} for $B^+ \to D\rho$ candidates reconstructed in official exp7 proc9 data.
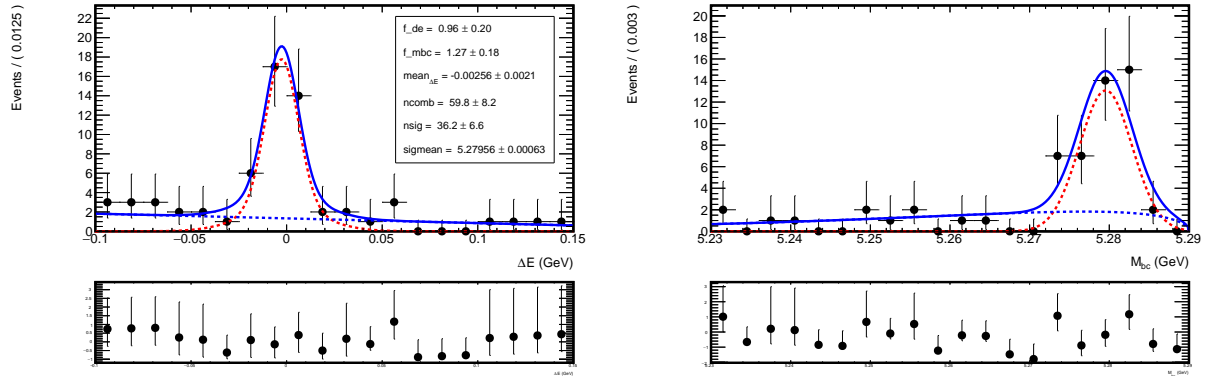
FIG. 40: Distributions of (left) ΔE and (right) and M_{bc} for $B^+ \to D^{*0}\pi$ candidates reconstructed in official exp7 proc9 data.
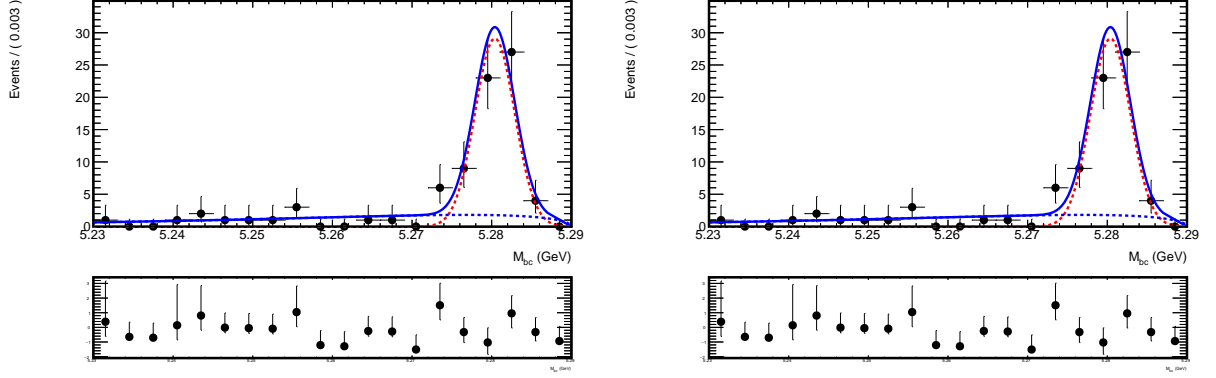
FIG. 41: Distributions of (left) ΔE and (right) M_{bc} for $B^0 \to D^{*\pm}\pi$ candidates reconstructed in official exp7 proc9 data.
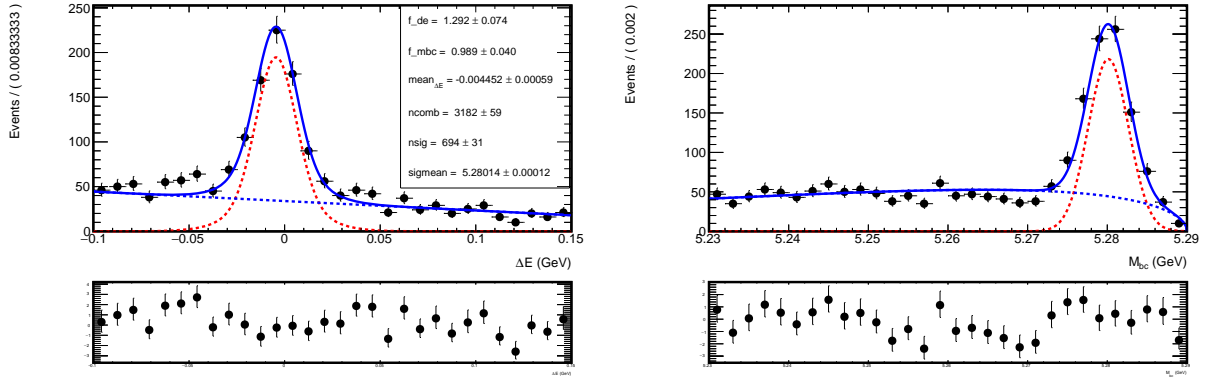
FIG. 42: Distributions of (left) ΔE and (right) and M_{bc} for $B^+ \to D\pi$ candidates reconstructed in official exp8 proc9 data.
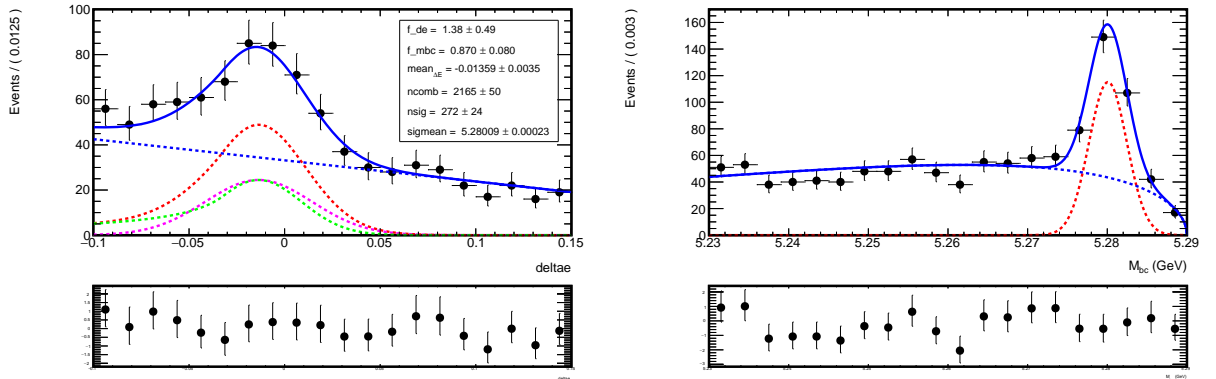
FIG. 43: Distributions of (left) ΔE and (right) and M_{bc} for $B^+ \to D\rho$ candidates reconstructed in official exp8 proc9 data.

25
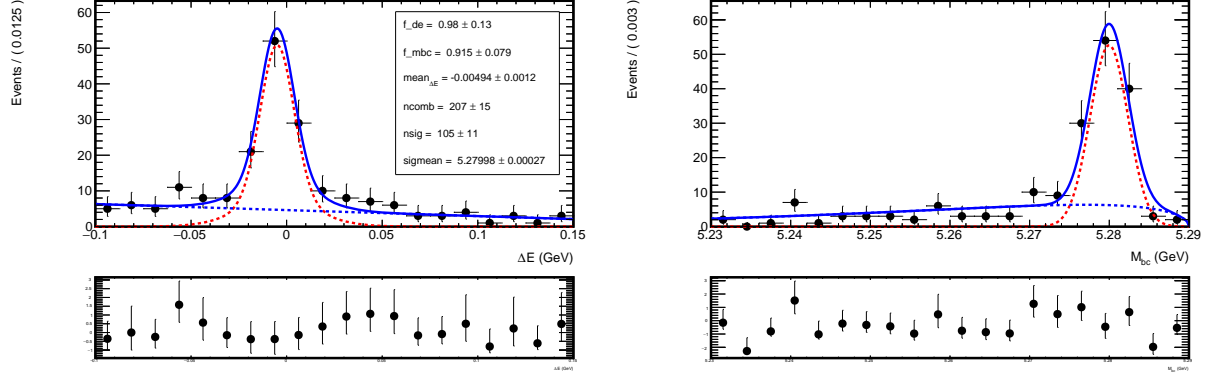
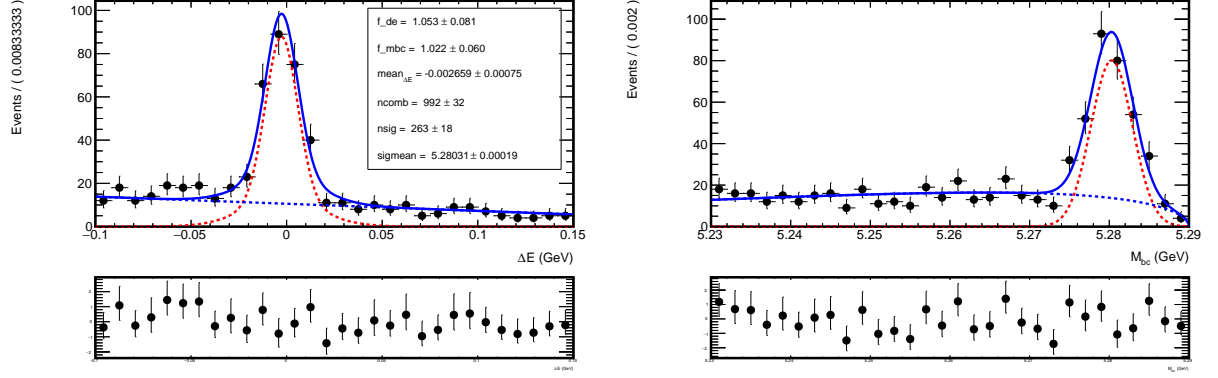FIG. 44: Distributions of (left) ΔE and (right) and M_{bc} for $B^+ \to D^{*0}\pi$ candidates reconstructed in official exp8 proc9 data.

FIG. 45: Distributions of (left) ΔE and (right) M_{bc} for $B^0 \to D^{*\pm}\pi$ candidates reconstructed in official exp8 proc9 data.

A RooPlot of "M$_{bc}$ (GeV/c^2)"

bckg_yield = 242 ± 16
frac_de = 0.113 ± 0.047
fudge = 1.36 ± 0.21
fudge_mbc = 0.828 ± 0.089
mean = 5.28095 ± 0.00034
mean3 = -0.00657 ± 0.0021
signal_yield = 73.1 ± 9.8

A RooPlot of "ΔE (GeV)"

FIG. 46: Distribution of ΔE and M_{bc} for $B^0 \to D^-(K^+\pi^-\pi^-)\pi^+$ candidates reconstructed in exp7 proc9 data.

A RooPlot of "M$_{bc}$ (GeV/c^2)"

bckg_yield = 12.1 ± 3.5
frac_de = 0.02 ± 0.63
signal_yield = 3.9 ± 2.0

A RooPlot of "ΔE (GeV)"

FIG. 47: Distribution of ΔE and M_{bc} for $B^0 \to D^-(K_S^0\pi^-)\pi^+$ candidates reconstructed in exp7 proc9 data.

A RooPlot of "M_{bc} (GeV/c^2)"

bckg_yield = 272 ± 18
frac_de = 0.50 ± 0.13
mean = 5.28057 ± 0.00061
signal_yield = 42.8 ± 9.0

A RooPlot of "ΔE (GeV)"

FIG. 48: Distribution of ΔE and M_{bc} for $B^0 \to D^-(K^+\pi^-\pi^-)\rho^+$ candidates reconstructed in exp7 proc9 data.

A RooPlot of "M_{bc} (GeV/c^2)"

bckg_yield = 757 ± 29
frac_de = 0.032 ± 0.026
fudge = 1.145 ± 0.090
fudge_mbc = 0.938 ± 0.061
mean = 5.28061 ± 0.00022
mean3 = -0.002592 ± 0.00096
signal_yield = 228 ± 17

A RooPlot of "ΔE (GeV)"

FIG. 49: Distribution of ΔE and M_{bc} for $B^0 \to D^-(K^+\pi^-\pi^-)\pi^+$ candidates reconstructed in exp8 proc9 data.

28

FIG. 50: Distribution of ΔE and M_{bc} for $B^0 \to D^-(K^0_S\pi^-)\pi^+$ candidates reconstructed in exp8 proc9 data.
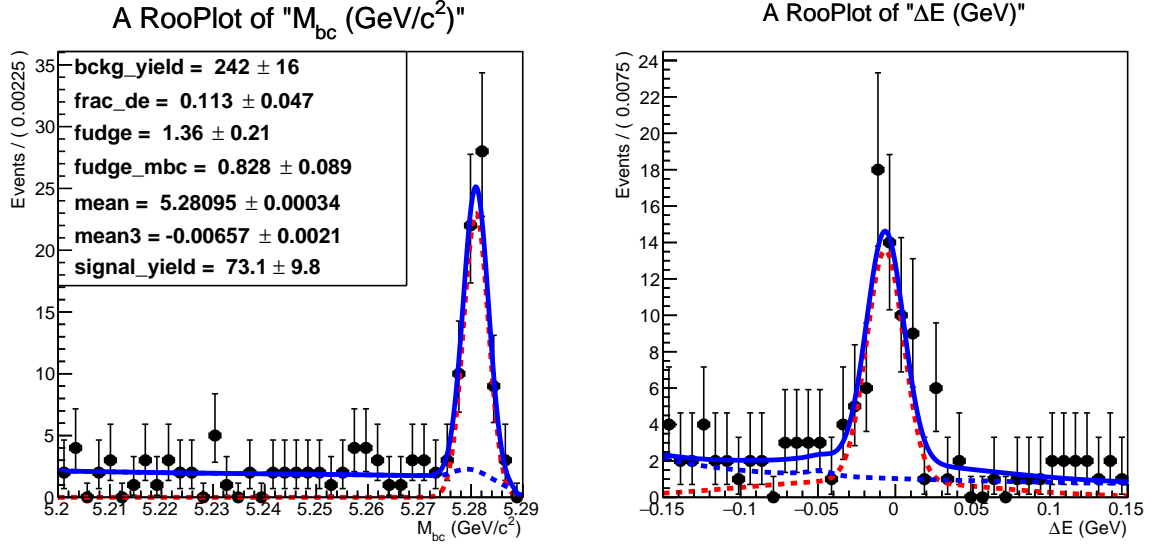

FIG. 51: Distribution of ΔE and M_{bc} for $B^0 \to D^-(K^+\pi^-\pi^-)\rho^+$ candidates reconstructed in exp8 proc9 data.
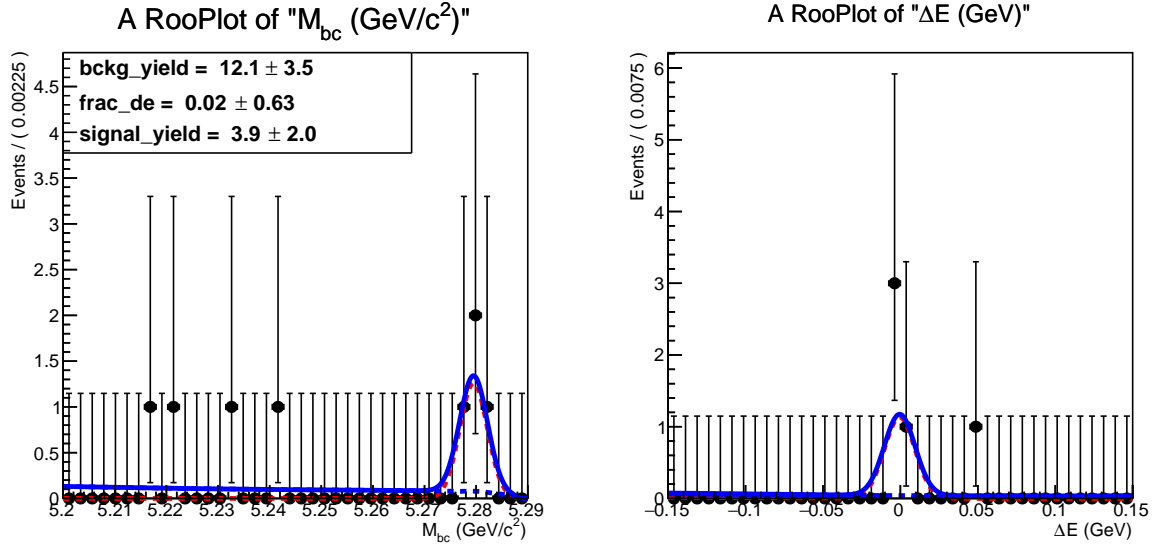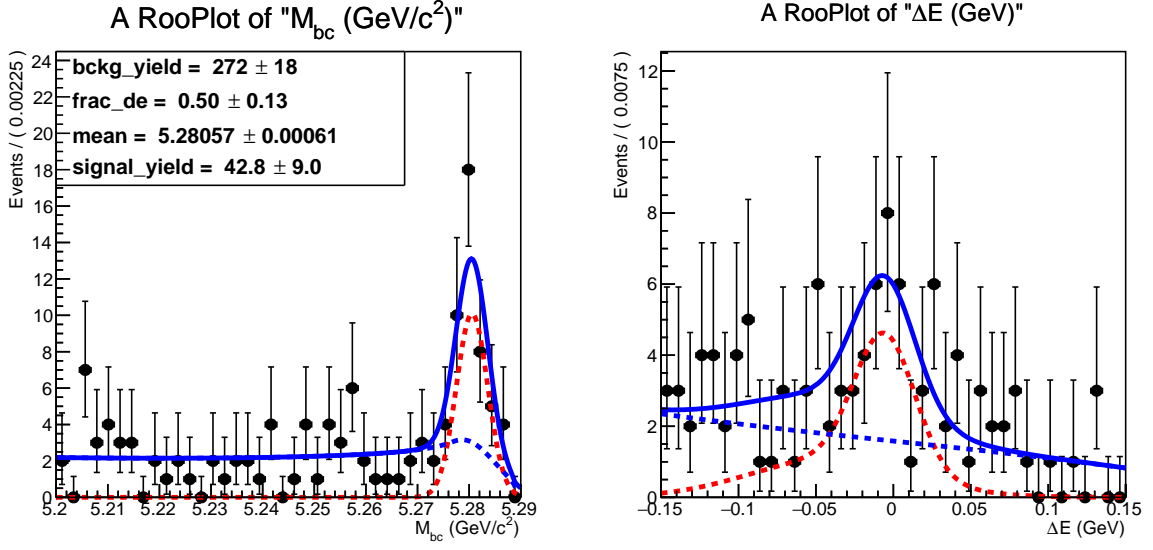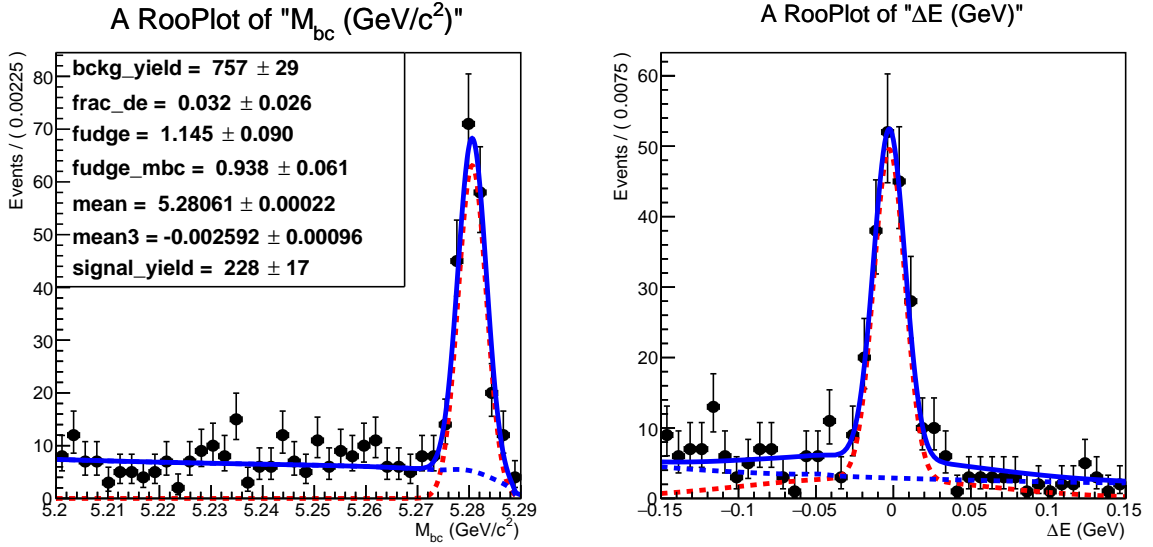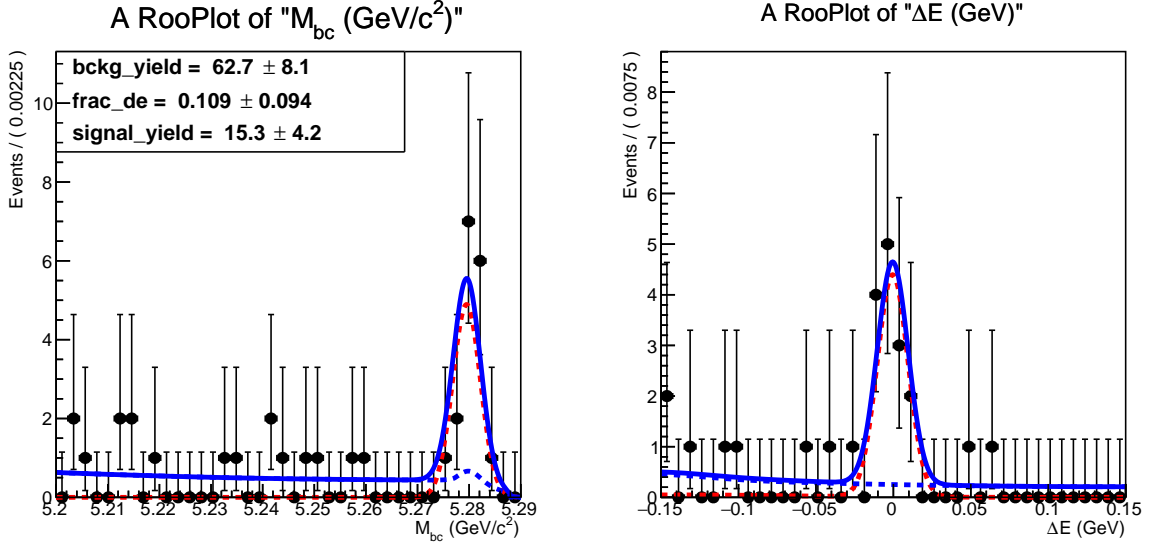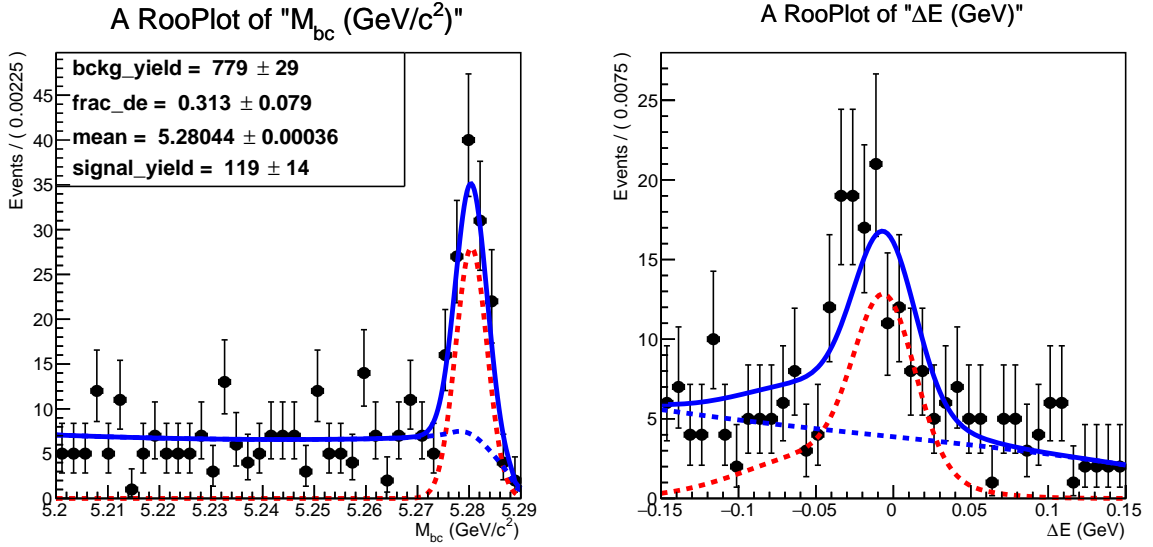
6.   COMPARISON WITH SIMULATION

Signal yields and purities in data are sufficient for allowing first quantitative comparison with the simulation. Table I compares signal yields in MC12 simulation, phase II data, and phase III (bucket6 only, bucket4+bucket6, exp8 unofficial, and official exp7+exp8 proc9) data. While signal yields per luminosity are increased with respect to phase II, we still observe 10–20% lower yields in data as compared to simulation for most modes, and 50% lower yields for $B^+ \to D\rho^+$ modes. The reason for the latter large discrepancy is under investigation. Comparison of exp7 and unofficial exp8 show consistent signal yields, indicating that variations in overall detector/condition calibrations are already quite small.

Table V shows a comparison between $B \to D\pi$ signal locations and widths in data and simulation. In data, we observe signal positions shifted by 1.6 MeV and ≈ 5 MeV in width in exp7 and exp8, respectively. A worsening of resolution is observed in unofficial exp8, as expected because of outdated calibrations.

	MC	Phase II	Exp7 (bucket6)	Exp7 (offic)	Exp8 (43-2249)	Exp7proc9	Exp8proc 9
Luminosity	1 fb^{-1}	472 pb^{-1}	344 pb^{-1}	413 pb^{-1}	1.8 fb^{-1}	0.69 fb^{-1}	2 fb^{-1}
$B \to D\pi$	437 ± 7	116	116 ± 12	140 ± 13	603 ± 29	263 ± 18	694 ± 31
$B \to D\rho$	285 ± 7	61	–	58 ± 11	222 ± 25	104 ± 14	272 ± 24
$B \to D^{*0}\pi$	83 ± 3	22	20 ± 5	24 ± 5	78 ± 10	36 ± 7	105 ± 11
$B^0 \to D^{*\pm}\pi$	128 ± 3	13	30 ± 5	32 ± 6	152 ± 13	62 ± 8	182 ± 14
$B^0 \to D^-\pi^+$	124 ± 4	25	31 ± 7	31 ± 7	215 ± 18	73 ± 10	228 ± 17
$B^0 \to D^-\rho^+$	67 ± 4	11	14 ± 6	15 ± 7	81 ± 15	43 ± 9	119 ± 14

TABLE I: Observed signal yields in data and simulation.

	MC	Phase II	Exp7 (offic)	Exp8 (43-2249)	Exp7proc9	Exp8proc9
$B \to D\pi$	437 ± 7	245	341 ± 31	335 ± 16	386 ± 26	347 ± 15
$B \to D\rho$	285 ± 7	129	141 ± 26	123 ± 14	152 ± 20	136 ± 12
$B \to D^{*0}\pi$	83 ± 3	46	58 ± 12	43 ± 6	53 ± 10	52 ± 5
$B^0 \to D^{*\pm}\pi$	128 ± 3	27	78 ± 14	84 ± 7	89 ± 12	91 ± 7
$B^0 \to D^-\pi^+$	124 ± 4	52	76 ± 17	119 ± 10	106 ± 14	114 ± 9
$B^0 \to D^-\rho^+$	67 ± 4	23	34 ± 17	45 ± 8	62 ± 14	60 ± 7

TABLE II: Signal yields per unit of integrated luminosity (in inverse femtobarns) in data and simulation.

	MC	Exp7 (official)	Exp8 (43-2249)
$K\pi$	96 ± 3	85 ± 14	77 ± 7
$K\pi\pi^0$	145 ± 4	100 ± 17	135 ± 10
$K\pi\pi\pi$	197 ± 5	156 ± 21	125 ± 10

TABLE III: Signal yields per unit of integrated luminosity (in inverse femtobarns) in data and simulation for various D final states in $B \to D\pi$.

Final states	MC	proc9
$K\pi$	1.45 ± 0.07	1.32 ± 0.148
$K\pi\pi^0$	0.31 ± 0.01	0.28 ± 0.02
$K\pi\pi\pi$	0.28 ± 0.008	0.17 ± 0.01

TABLE IV: Signal-to-background ratios for various D final states in $B \to D\pi$ decays reconstructed in simulated and proc9 data and selected with a pionID > 0.4 requirement to mimic DK yields.

	MC12	exp7 (bucket4,6)	exp8 (unofficial)
Luminosity	10 fb^{-1}	0.41 fb^{-1}	1.8 fb^{-1}
Mean$_{\Delta E}$ (GeV)	-0.000194 ± 0.00018	-0.00214 ± 0.0011	-0.005317 ± 0.00065
$\sigma_{\Delta E}/f_{\Delta E}$ (GeV)	$\mathbf{0.00798 \pm 0.00016}$	1.09 ± 0.11	1.327 ± 0.081
Mean$_{M_{bc}}$ (GeV/c^2)	5.279188 ± 0.000046	5.28014 ± 0.00023	5.28020 ± 0.00013
$\sigma_{M_{bc}}/f_{M_{bc}}$ (GeV/c^2)	$\mathbf{0.002554 \pm 0.000037}$	0.888 ± 0.075	0.973 ± 0.040

TABLE V: Signal-peak parameters for $B \to D\pi$ decays reconstructed in data and simulation. $f_{\Delta E}$ and $f_{M_{bc}}$ are the fudge factor on ΔE and M_{bc} resolution in data.

	exp7 (proc8)	exp7 (proc9)
Luminosity	0.41 fb^{-1}	0.69 fb^{-1}
Mean$_{\Delta E}$ (GeV)	-0.00214 ± 0.0011	0.002659 ± 0.00075
$f_{\Delta E}$ (GeV)	1.09 ± 0.11	1.053 ± 0.081
Mean$_{M_{bc}}$ (GeV/c^2)	5.28014 ± 0.00023	5.28031 ± 0.00019
$f_{M_{bc}}$ (GeV/c^2)	0.888 ± 0.075	1.022 ± 0.060

TABLE VI: Signal peak parameters for $B \to D\pi$ decays reconstructed in official proc8-exp7 and proc9-exp7 data.

	exp7 (proc8)	exp7 (proc9)
Luminosity	1.8 fb^{-1}	2.0 fb^{-1}
Mean$_{\Delta E}$ (GeV)	-0.005317 ± 0.00065	0.004452 ± 0.00059
$f_{\Delta E}$ (GeV)	1.327 ± 0.081	1.292 ± 0.074
Mean$_{M_{bc}}$ (GeV/c^2)	5.28020 ± 0.00013	5.28014 ± 0.00012
$f_{M_{bc}}$ (GeV/c^2)	0.973 ± 0.040	0.989 ± 0.040

TABLE VII: Signal-peak parameters for $B \to D\pi$ decays reconstructed in unofficial exp8 and official proc9-exp8 data.

7. $B \to DK$ IN DATA

7.1.   EPS data

The high yield observed in $B \to D\pi$ decays suggests that its Cabibbo-suppressed counterpart $B \to DK$ could be visible too in our full exp7+exp8 data set corresponding to 2.2 fb^{-1}. The $B \to DK$ decay is the principal channel used for the measurement of ϕ_3/γ and observing it would offer important information for assessing PID and mass-resolution performances. Simulation suggests that by inverting the pionID < 0.6 requirement originally imposed on the pion from the B decay, a distinctive $B \to DK$ peak ought be visible (Figure 52). This is confirmed in data, where two adjacent peaking structures are visible: the peak centered at $\Delta E \approx 0$ are the dominant $B \to D\pi$ decays reconstructed with a misidentified pion, the other peak at $\Delta E \approx -0.5$ represents the first evidence in Belle II data for $B \to DK$ decays (Fig. 53).
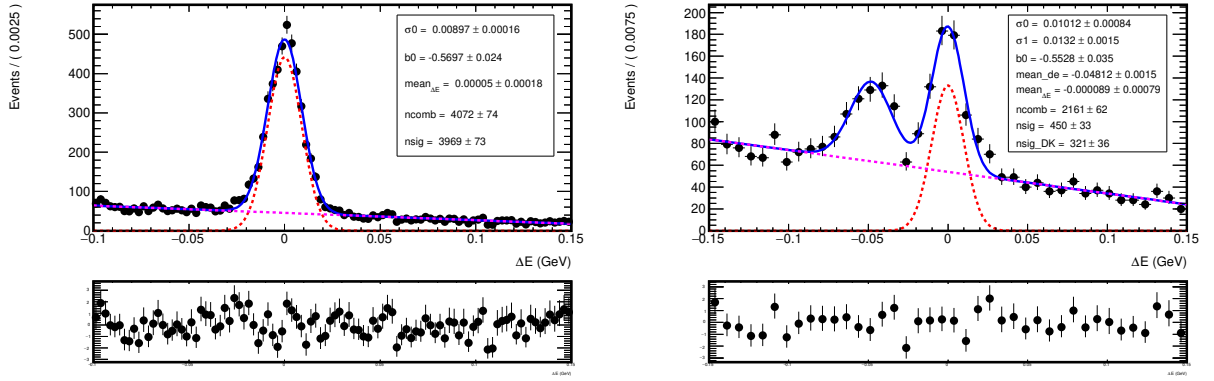

FIG. 52: Distribution of ΔE for simulated $B \to D\pi$ candidates selected with the (left) pionID $>$ 0.6 and (right) pionID < 0.6 requirement with fit projections overlaid and pulls.

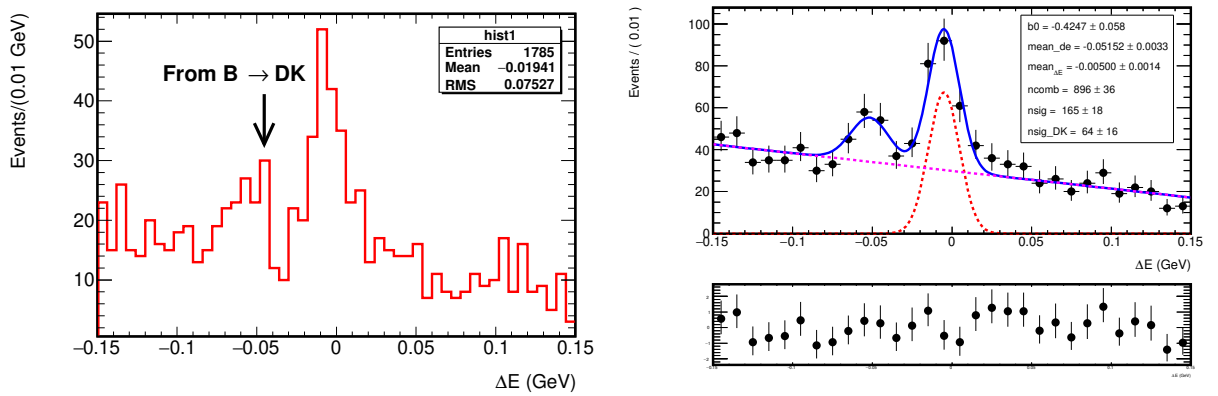

FIG. 53: Distributions of ΔE for $B \to D\pi$ decays selected with the pionID < 0.6 requirement and reconstructed in expt7+expt8 data (2.2 fb^{-1}).

33

7.2. Lepton Photon data

Our main goal with the proc9 data sample is to benchmark the Belle II performance in reconstructing a solid $B \to DK$ signal. To achieve that, we invert the PID requirement on the track from the B candidate (prompt track) to enrich the prompt-track in kaons and use improved continuum suppression as described in Section 3.

Figure 54 shows the ΔE distribution of $B^+ \to D\pi^+$ candidates reconstructed in simulated and proc9 experimental data, selected through the baseline plus continuum-suppression selection, a requirement of PID<0.4 on the track from B and further restricted to $M_{\mathrm{bc}} >$ 5.27 GeV/c^2. We fit the one-dimensional ΔE distribution with the sum of two Gaussian distributions with fixed widths, and apply a fudge factor on the narrow-Gaussian width, whose value is fixed from the $D\pi$ fit. The background is a floating exponential. The fit determines the mean of the signal, the signal yield, and the background slope. A prominent $B \to DK$ peak is clearly visible. The statistical significance of the signal, based on the Wilks' theorem and assuming that the likelihood-ratio between the signal-plus-background and background-only hypotheses is distributed as a χ^2 exceeds 5.0 Gaussian standard deviations.

In order to demonstrate the presence of a $B^+ \to DK$ signal independent of the kaon-enriching PID requirement, we show the same distribution without any PID requirement on the prompt track (Fig. 55, right panel) and with a pion-enriching requirement PID > 0.4 on the track from B (Fig. 55, left panel).

Figure 56 shows the ΔE distribution of $B^0 \to D^-\pi^+$ candidates reconstructed in simulated and proc9 experimental data, selected through the baseline plus continuum-suppression selection, a requirement of PID<0.4 on the track from B, and further restricted to $M_{\mathrm{bc}} > 5.27$ GeV/c^2. We fit the one-dimensional ΔE distribution with the sum of two Gaussian distributions, one for $D\pi$ and another for DK. The mean of the $D\pi$ Gaussian is floating and the distance of the DK mean from it is fixed from simulation as are the widths. The background is modeled witha 2nd-order polynomial fixed from simulation. A prominent $B \to DK$ peak is clearly visible. The statistical significance of the signal, based on the Wilks' theorem and assuming the likelihood-ratio distributed as a χ^2 is 4.0 Gaussian standard deviations.

In order to demonstrate the presence of a $B^0 \to DK$ signal independent of kaon-enriching PID requirements, we show the same distribution without any PID requirement on the prompt track (Fig. 57, right panel) and with a pion-enriching requirement PID > 0.4 on the track from B (Fig. 55, left panel).

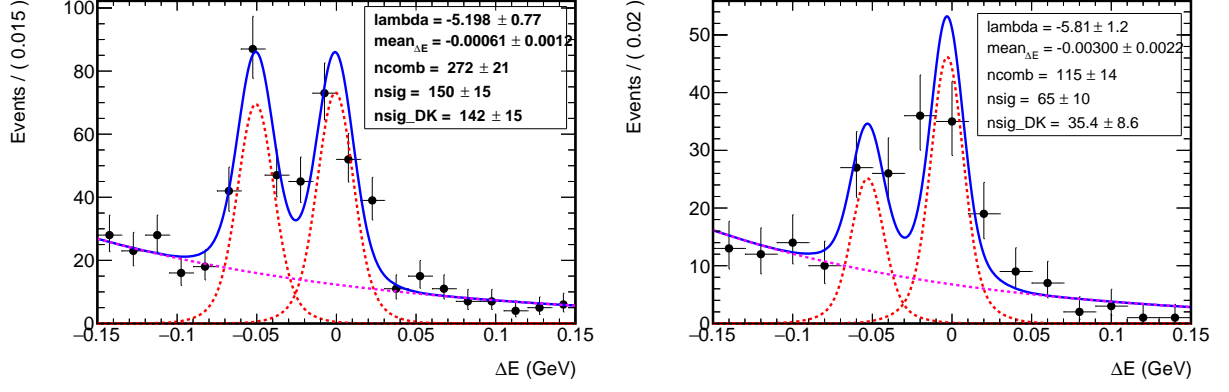FIG. 54: Distributions of a ΔE for $B^+ \to D\pi^+$ candidates reconstructed in (left) simulated and (right) proc9 experimental data, selected through the baseline plus continuum-suppression selection, a kaon-enriching requirement of PID < 0.4 on the prompt track, and further restricted to $M_{\rm bc} > 5.27$ GeV/c^2. Fit projections are overlaid.
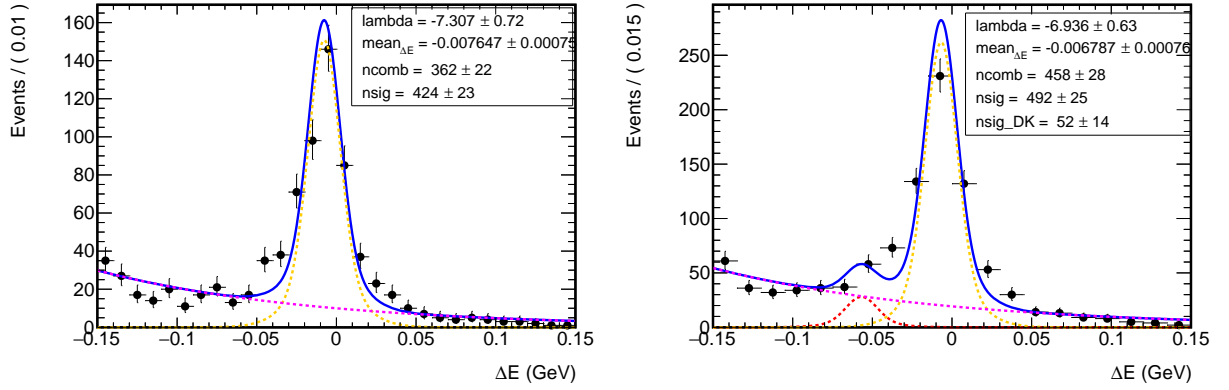

FIG. 55: Distributions of a ΔE for $B^+ \to D\pi^+$ candidates reconstructed proc9 experimental data, selected through the baseline plus continuum-suppression selection, further restricted to $M_{\rm bc} > 5.27$ GeV/c^2, and with (left) a pion-enriching requirement of PID > 0.4 on the prompt track, or (right) no PID requirement on the prompt track. Fit projections are overlaid.
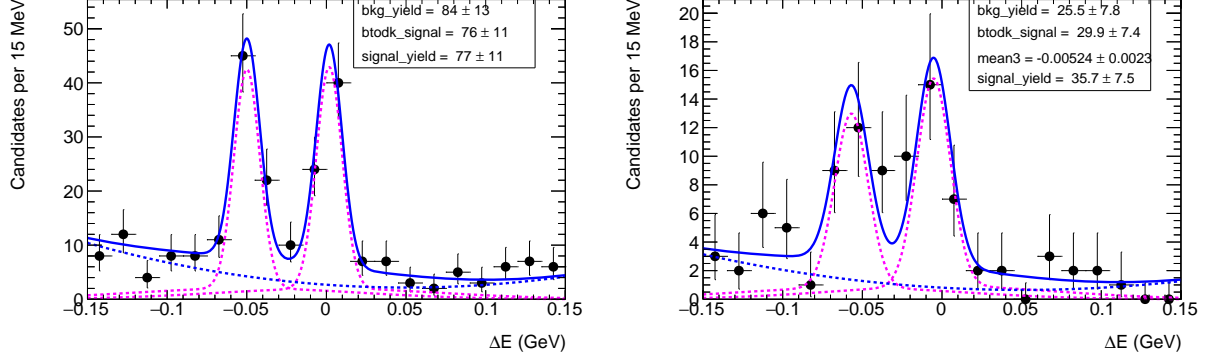
FIG. 56: Distributions of a ΔE for $B^0 \to D\pi$ candidates reconstructed in (left) simulated and (right) proc9 experimental data, selected through the baseline plus continuum-suppression selection, a kaon-enriching requirement of PID <0.4 on the prompt track, and further restricted to $M_{\text{bc}} > 5.27$ GeV/c^2. Fit projections are overlaid.
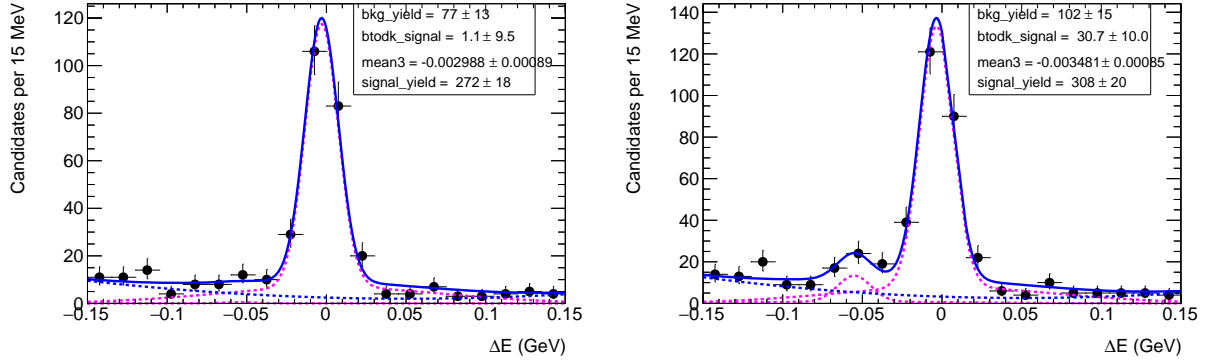

FIG. 57: Distributions of a ΔE for $B^0 \to D\pi$ candidates reconstructed proc9 experimental data, selected through the baseline plus continuum-suppression selection, further restricted to $M_{\text{bc}} > 5.27$ GeV/c^2, and with (left) a pion-enriching requirement of PID > 0.4 or (right) no PID requirement on the prompt track. Fit projections are overlaid.

8. DETERMINATION OF THE BEAM-ENERGY SPREAD

We determine the beam-energy spread from a fit of the M_{bc} distribution for the high-yield decay $B^+ \to D\pi$. The observed width of M_{bc} approximates the energy spread assuming negligible the uncertainty on B-meson momentum in the center-of-mass system. Figure 58 shows the corresponding M_{bc} distributions in exp7 and exp8 data, respectively, with fit projections overlaid. We use a Gaussian function to model signal and an Argus function for the background in the one-dimensional fit shown in Fig. 58. Table VIII shows the resolution and shift in peak position observed in exp7 and exp8 data, compared to simulation. The shift is approximately 1 MeV for both data sets.
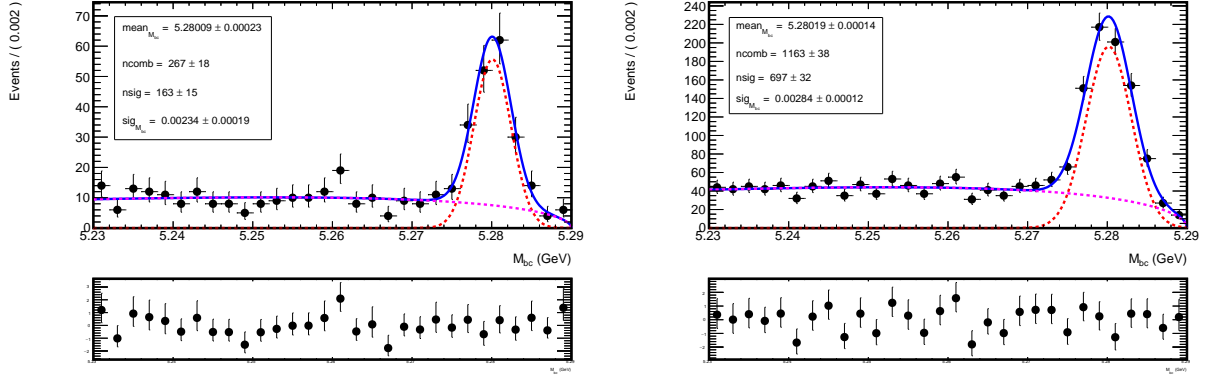

FIG. 58: Distribution of M_{bc} for $B \to D\pi$ decays reconstructed in (left) exp7-bucket6 and (right) exp8 data.

	MC12	Exp7 (bucket6)	Exp8
Mean$_{M_{bc}}$ (GeV/c^2)	5.2791 ± 0.0000	5.2800 ± 0.0002	5.2802 ± 0.0001
Shift (MeV/c^2)	0	0.9	1.1
$\sigma_{M_{bc}}$ (GeV/c^2)	0.002696 ± 0.000045	0.00234 ± 0.00019	0.00284 ± 0.00012

TABLE VIII: Widths and positions of the M_{bc} peak of $B \to D\pi$ decays for experimental and simulated data.

	Exp7 (proc9)	Exp8 (proc9)
Mean$_{M_{bc}}$ (GeV/c^2)	5.28031 ± 0.00019	5.28014 ± 0.00012
Shift (MeV/c^2)	1.2	1.0
$\sigma_{M_{bc}}$ (GeV/c^2)	0.00261 ± 0.00015	0.00253 ± 0.00010

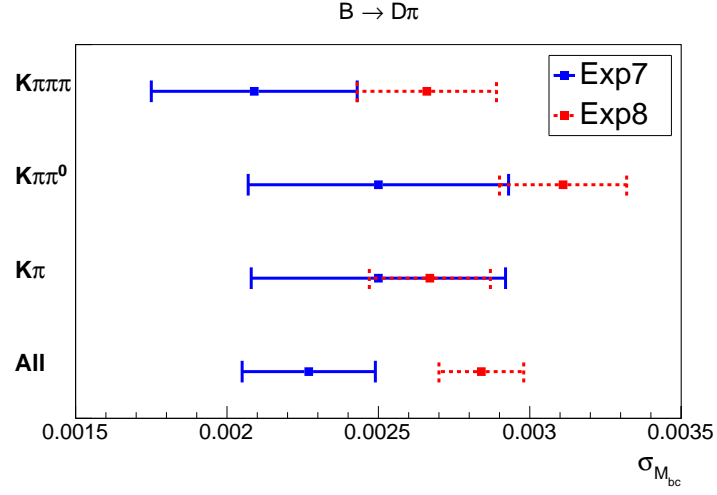TABLE IX: Widths and positions of the M_{bc} peak of $B^+ \to D\pi$ decays for proc9 data.

FIG. 59: Beam energy spread for various $B^+ \to D\pi$ final states in exp7 (bucket6) data and exp8 unofficial data.

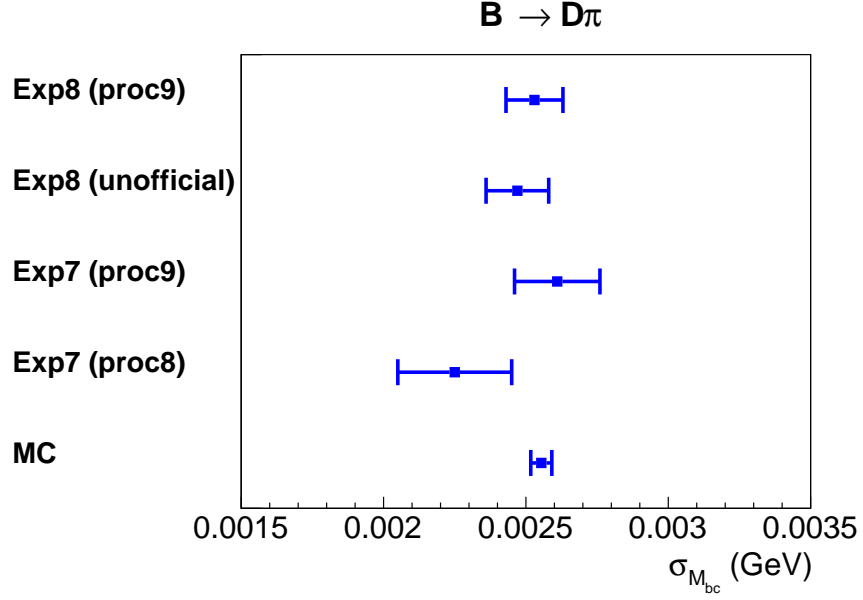FIG. 60: Beam energy spreads for various reprocessing as determined using $B^+ \to D\pi$ decays.

9. $B^{\pm} \to D(K_S^0 \pi^+ \pi^-)\pi^{\pm}$ IN PROC9 DATA

Reconstruction of $B^{\pm} \to D(K_S^0 \pi^+ \pi^-)\pi^{\pm}$ decays is a particularly relevant benchmark as this is a golden mode for ϕ_3 determination. We reconstruct $B^{\pm} \to D(K_S^0 \pi^+ \pi^-)\pi^{\pm}$ candidates in proc9 data with the selection outlined in Section 2 along with the `goodKs` selection. Figure 62 and 63 show the ΔE and M_{bc} distributions with fit projections overlaid. Here, we use the same signal and background fit model as of $D\pi$.
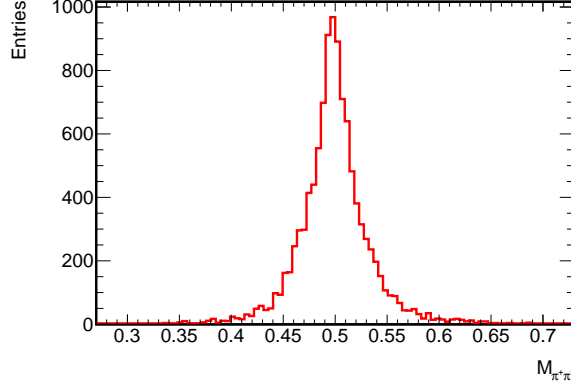

FIG. 61: K_S^0 mass distribution in proc9 data from the reconstruction of $B^{\pm} \to D(K_S^0 \pi^+ \pi^-)\pi^{\pm}$ with `goodKs` selection
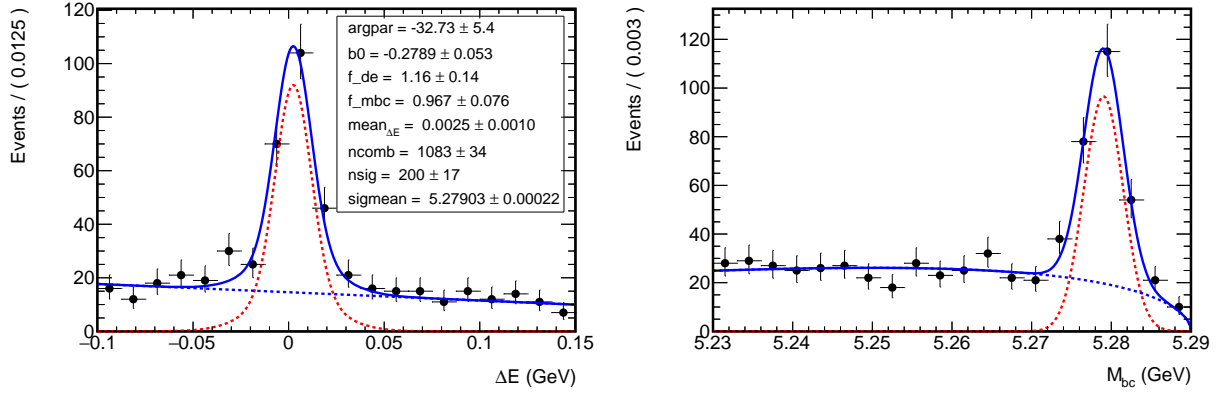

FIG. 62: Distributions of (left) ΔE and (right) M_{bc} for $B^{\pm} \to D(K_S^0 \pi^+ \pi^-)\pi^{\pm}$ candidates reconstructed in MC12.
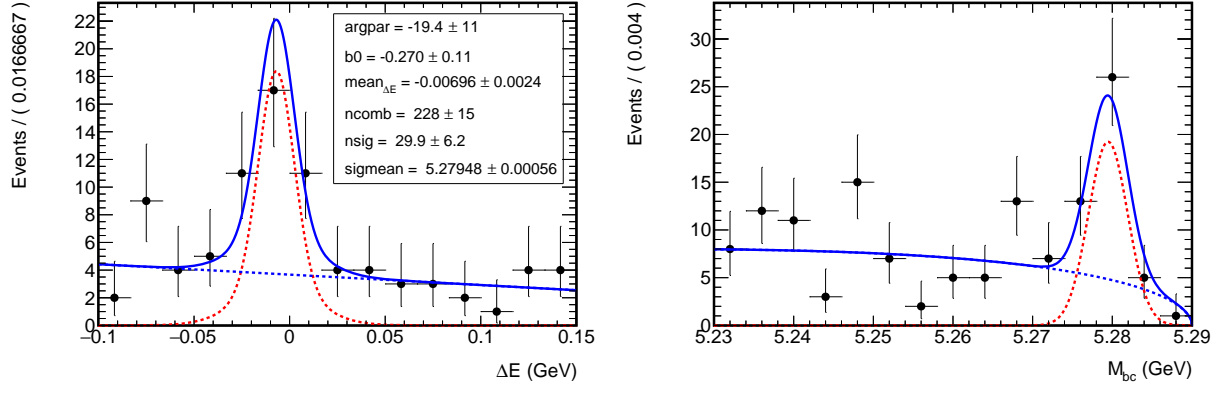
39

FIG. 63: Distributions of (left) ΔE and (right) M_{bc} for $B^{\pm} \to D(K^0_S \pi^+ \pi^-)\pi^{\pm}$ candidates reconstructed in proc9 data with fit projections overlaid.

10. MATERIAL FOR EPS

Figure 64 shows the ΔE and M_{bc} distribution of all B candidates reconstructed in the exp7 official data set corresponding to 410 pb^{-1}. These plots are formatted for public showing at the EPS 2019 conference.
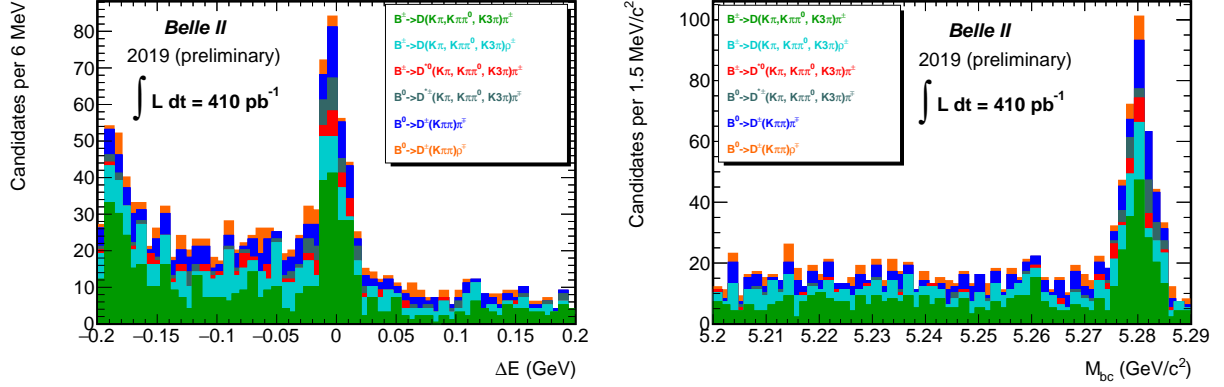

FIG. 64: Distributions of (left) ΔE and (right) M_{bc} for all the B candidates reconstructed in official exp7 data of 410 pb^{-1}. The ΔE distribution is made by restricting the candidates to the signal region in M_{bc} and viceversa. Plots are formatted for public showing at EPS.

11. MATERIAL FOR LP

Figure 65 shows the ΔE and M_{bc} distribution of all B candidates reconstructed in the proc9 official data set corresponding to 2.7 fb^{-1}. The ΔE distribution is made by restricting the candidates to the signal region in M_{bc} and viceversa. These plots are formatted for public showing at the LP 2019 conference.

12. TO BE ADDED SOON

- $M(\pi\pi)$ from MC (to be overlaid on current Fig.61)

- yields in different D modes

- update figs 55, 56, 57, 58 (proper colors, remove "A Rooplot...")

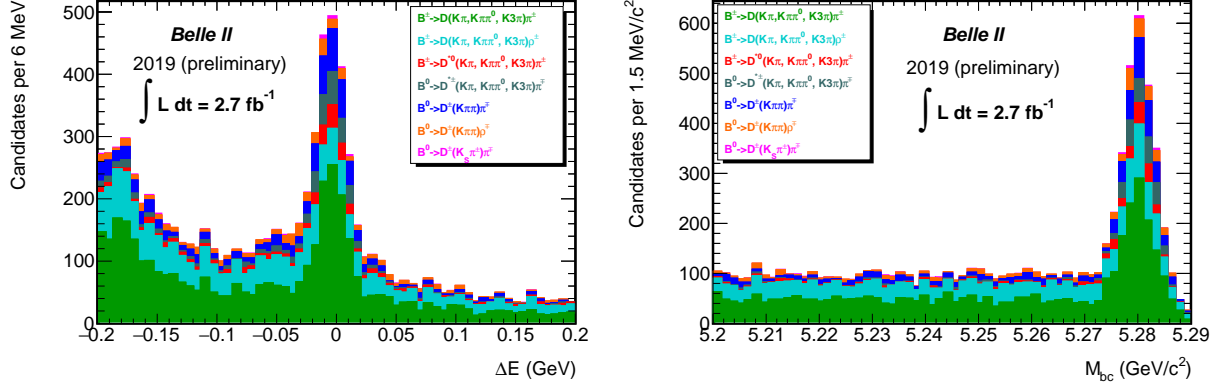- average multiplicity

- K_s^0 study

- ...

FIG. 65: Distributions of (left) ΔE and (right) M_{bc} for all the B candidates reconstructed in official proc9 data of 2.7 fb^{-1}. The ΔE distribution is made by restricting the candidates to the signal region in M_{bc} and viceversa. Plots are formatted for public showing at LP.

13. SUMMARY

We validate early phase III data using hadronic B decays. We reconstruct prominent signals for a variety of $B \to Dh$ decays. A total signal yield of approximately 300 decays is reconstructed in a sample (exp7) corresponding to 0.410 fb^{-1} and proposed for public showing at the EPS 2019 conference. Addition of further data (exp8) and a novel processing (proc9) allows to reconstruct a total of 2200 decays in 2.69 fb^{-1}, proposed for public showing at the Lepton Photon 2019 conference. This includes observation of the Cabibbo-suppressed $B \to DK$ signal in Belle II data. Study of these signals allows for determining the beam-energy spread from data with approximately 5% precision. Signal yields are moderately (10–20%) inferior to those expected from simulation, with comparable backgrounds, but superior to those obtained in the 2018 pilot commissioning run. These result show a remarkable level of early understanding of detector performance in hadronic final-state reconstruction.